The FEBS Journal

FEBS PRESS science publishing by scientists

Fusion–fission–mitophagy cycling and metabolic reprogramming coordinate nerve growth factor (NGF)-dependent neuronal differentiation

Ilaria Goglia[1], Ewelina Węglarz-Tomczak[2,*], Claudio Gioia[1], Yanhua Liu[2], Assunta Virtuoso[3], Marcella Bonanomi[4], Daniela Gaglio[4], Noemi Salmistraro[5], Ciro De Luca[3], Michele Papa[3,5], Lilia Alberghina[5,6], Hans V. Westerhoff[2,6,7,8,9] and Anna Maria Colangelo[1,5,6,10]

1 Laboratory of Neuroscience "R. Levi-Montalcini", Department of Biotechnology and Biosciences, University of Milano-Bicocca, Milano, Italy
2 Synthetic Systems Biology and Nuclear Organization, Swammerdam Institute for Life Sciences, University of Amsterdam, The Netherlands
3 Laboratory of Morphology of Neuronal Network, Department of Public Medicine, University of Campania "Luigi Vanvitelli", Napoli, Italy
4 Institute of Molecular Bioimaging and Physiology (IBFM), National Research Council (CNR), Segrate, Italy
5 SYSBIO Centre of Systems Biology ISBE.ITALY, University of Milano-Bicocca, Italy
6 Infrastructure for Systems Biology Europe (ISBE), Amsterdam, The Netherlands
7 Molecular Cell Physiology, VU University Amsterdam, The Netherlands
8 Faculty of Biology, Medicine and Health, School of Biological Sciences, University of Manchester, UK
9 Stellenbosch Institute for Advanced Study (STIAS), Wallenberg Research Centre at Stellenbosch University, South Africa
10 NeuroMI Milan Center for Neuroscience, University of Milano-Bicocca, Italy

Keywords
computational modeling; metabolism; mitochondrial dynamics; mitophagy; NGF differentiation

Correspondence
A. M. Colangelo, Laboratory of Neuroscience "R. Levi-Montalcini", Department of Biotechnology and Biosciences, University of Milano-Bicocca, piazza della Scienza 2, Milano, Italy
Tel: +390264483536
E-mail: annamaria.colangelo@unimib.it
and
H. V. Westerhoff, Molecular Cell Physiology, Faculty of Science, VU University, De Boelelaan 1108, Amsterdam, The Netherlands
Tel: +272118083874; +31206143163
E-mail: h.v.westerhoff@vu.nl; h.v.westerhoff@uva.nl

Neuronal differentiation is regulated by nerve growth factor (NGF) and other neurotrophins. We explored the impact of NGF on mitochondrial dynamics and metabolism through time-lapse imaging, metabolomics profiling, and computer modeling studies. We show that NGF may direct differentiation by stimulating fission, thereby causing selective mitochondrial network fragmentation and mitophagy, ultimately leading to increased mitochondrial quality and respiration. Then, we reconstructed the dynamic fusion–fission–mitophagy cycling of mitochondria in a computer model, integrating these processes into a single network mechanism. Both the computational model and the simulations are able to reproduce the proposed mechanism in terms of mitochondrial dynamics, levels of reactive oxygen species (ROS), mitophagy, and mitochondrial quality, thus providing a computational tool for the interpretation of the experimental data and for future studies aiming to detail further the action of NGF on mitochondrial processes. We also show that changes in these mitochondrial processes are intertwined with a metabolic function of NGF in differentiation: NGF directs a profound metabolic rearrangement involving glycolysis, TCA cycle, and the pentose phosphate pathway, altering the redox balance. This

Abbreviations
Baf, bafilomycin A1; CC, AMPK inhibitor Compound C; D, healthy dispersed mitochondria; Dd, mild damaged dispersed mitochondria; Ddd, severely damaged dispersed mitochondria; GAP43, growth-associated protein 43; Glc, glucose; Gln, glutamine; Glu, glutamate; GSH, reduced Glutathione; GSSG, oxidized Glutathione; H_2DCF-DA, dichloro-dihydrofluoresceine diacetate; JNKi, c-Jun N-terminal kinase inhibitor; LC–MS, Liquid chromatography-mass spectrometry; LTR, LysoTracker red; MFI, mean fluorescence intensity; MTG, MitoTracker Green; MTR, MitoTracker Red CMXRos; N, healthy networked mitochondria; NAD^+, nicotinamide adenine dinucleotide; Nd, mild damaged networked mitochondria; Ndd, severely damaged networked mitochondria; NGF, nerve growth factor; PI3K, phosphoinositol-3-kinase; PPP, pentose phosphate pathway; R5P, ribose-5-phosphate; RAP, rapamycin; ROS, reactive oxygen species; SOD1, superoxide dismutase 1; TCA cycle, tricarboxylic acid cycle; TOMM20, translocase of outer mitochondrial membrane 20; V_m, mitophagy (reaction); V_{ROSd}, degradation of ROS produced by Dd and Ddd (reaction); V_{rosd}, degradation of ROS produced by Nd and Ndd (reaction); V_{ROSs}, ROS synthesis by Dd and Ddd (reaction); V_{ross}, ROS synthesis by Nd and Ndd (reaction); V_s, mitochondria biogenesis (reaction); WT, wortmannin.

Present address
*NatInLab B.V., the Netherlands & Molecular Neuroscience, Swammerdam Institute for Life Sciences, Faculty of Science, University of Amsterdam, Amsterdam, The Netherlands

Ilaria Goglia, Ewelina Węglarz-Tomczak and Claudio Gioia contributed equally to the article

(Received 9 July 2023, revised 2 November 2023, accepted 29 January 2024)

doi:10.1111/febs.17083

metabolic rewiring may ensure: (a) supply of both energy and building blocks for the anabolic processes needed for morphological reorganization, as well as (b) redox homeostasis.

Introduction

Neuronal differentiation requires extensive modification of molecular and morphological properties to comply with the novel specialized functions. Neuronal branching also involves the remodeling of organelles, in particular mitochondria, as they need to spread into the growing neurites and sustain the high energy requirements essential for synapse formation and neurotransmission [1,2]. Several studies have recently addressed the contribution of mitochondrial dynamics and metabolism to neuronal development [3–9].

The mitochondrial morphology, of fragmented or highly interconnected networks, is controlled by the balance between fusion and fission in continuous cycles. Fusion, regulated by mitofusins1/2 (Mfn1/2) and optic atrophy-1 (Opa1), increases the rescue of damaged mitochondria and their metabolic efficiency. Fission, regulated by dynamin-related protein-1 (Drp1), favors the transport of dispersed mitochondria along neurites, as well as the removal of damaged mitochondria by mitophagy [10–12]. Indeed, mitochondrial dynamics is closely related to mitophagy in response to metabolic or environmental stresses that cause high production of Reactive Oxygen Species (ROS), byproducts of the oxidative mitochondrial respiration [13–16]. ROS cause oxidative damage to all mitochondrial components (lipid, proteins, and mtDNA), thus compromising the bioenergetic capacity of mitochondria and making them prone to further ROS production. This oxidative cycle is blocked by changes in mitochondrial dynamics through increased fission and decreased fusion, thereby promoting the quarantine of damaged fractions of mitochondria. Then, activation of mitophagy through multiple regulatory signaling effects the clearance of damaged or dysfunctional mitochondria in PINK/Parkin or BNIP3L/NIX-mediated pathways [11,17–21].

The entire process, essential for mitochondria quality control, is regulated at multiple levels [22]. Evidence suggests the reciprocal influence between the fission/fusion machinery and the mitochondrial/cellular bioenergetic status (i.e., mitochondrial membrane potential and ATP levels), as well as the regulation by Bcl-2 proteins and post-translational modifications [3,10,23]. Additional control of mitochondrial quality is provided by mitochondrial proteases, such as Omi/HtrA2 which plays a key role in processing Opa1 to maintain the balance of short and long isoforms required for mitochondria elongation [24]. Mitochondrial quality control is crucial for neuronal development, to maintain mitochondrial turnover and Gibbs energy homeostasis in the growing neurites engaged in axon remodeling during differentiation and neuroplasticity [9,12,25–27]. On the other hand, the dynamic changes of the mitochondria phenotype switch their metabolic pattern from glycolytic to oxidative phosphorylation resulting in increased ATP production [12,25,26], while producing more ROS [1,28].

Neuronal differentiation is initiated by complex intrinsic and extrinsic signaling pathways, such as in response to morphogens and/or trophic factors. Among them, Nerve Growth Factor (NGF) [29] is essential for neurogenesis and development of cholinergic neurons in the brain, as well as for sympathetic and sensory neurons in the peripheral nervous system [30–33]. The NGF/PI3K/Akt signaling plays a role in regulating the balance of pro- and anti-apoptotic Bcl-2 proteins, as well as the expression of ROS scavenging enzymes, such as the Cu/Zn-superoxide dismutase (Cu/Zn-SOD) [31,34], thus suggesting an effect on mitochondrial function and redox homeostasis.

Neuronal differentiation by NGF may be served by a transient dispersion of the mitochondria. In our

previous study of NGF-induced differentiation [12], we made some observations constraining the mechanisms that could be operative: NGF administration stimulated mitochondrial respiration and caused a transient rise in ROS levels and autophagy flux. These observations might be due to an enhanced metabolic workload imposed by the differentiation *per se*. The alternative of NGF fostering the mitophagy flux by increasing the fission rate is also likely, as supported by our observation of increased P-Drp1 [12], presumably through increased ROS and/or activation of PI3K and ERK1/2 signaling cascades [7], and the observation that inhibition of fission reduces NGF-induced axonal branching and differentiation [7].

To address these possibilities, we here show by time-lapse imaging that NGF-induced differentiation occurs with changes in mitochondrial dynamics and mitophagy, ultimately leading to increased mitochondrial quality. We then reconstruct the dynamic fusion–fission cycling of mitochondria in a computer model and relate this to mitophagy. That model helps us demonstrate how the fusion–fission cycling can serve to enhance the performance of mitochondria subject to ROS challenges. An increase in mitochondrial fission activity in the model causes a transient increase in ROS levels, as well as a permanent increase in mitochondrial activity, both phenomena confirmed experimentally upon induction of PC12 cell differentiation by NGF. Moreover, we provide evidence of the substantial metabolic changes involving glycolysis, TCA cycle, Pentose Phosphate pathway and redox balance. This metabolic reprogramming may be necessary to fulfill the energy demand, to drive anabolic processes in differentiation and manage the redox balance.

Together with the results reported in [12], these new results constitute a comprehensive dataset on how NGF regulates neuronal differentiation through its effects on mitochondrial dynamics. The integration of models and experimental data show how neuronal differentiation may work. They support the fusion–fission–mitophagy mechanism we propose for how NGF manages mitochondrial quality and dynamics, thereby ensuring the metabolic remodeling needed for the differentiation.

Results

NGF-induced differentiation occurs with increased mitochondrial fission and mitophagy to improve mitochondrial quality

We previously showed that NGF-induced differentiation occurs with changes in mitochondrial respiration, ROS production, P(Ser616)-DRP1 levels and autophagy flux as revealed by the GFP-RFP-LC3 fluorescence and levels of LC3 and p62 in the presence of autophagy inhibitors [12], suggesting that NGF might foster mitophagy by increasing the fission rate.

To further explore the impact of fission and mitophagy on neuronal differentiation, we here examined the effect of NGF on mitochondria populations and mitophagy by time-lapse imaging of PC12 cells stained by Mitotracker green (MTG) and Lysotracker red (LTR) [35]. As documented in Fig. 1A–E, NGF treatment increases the fraction of fragmented mitochondria: the 2–6 and 20–26 h time-lapse sequences show regions rich in dispersed mitochondria at 4–5 h and at 20–25 h (Fig. 1B,C, respectively, white arrows), as quantified in (Fig. 1E upper panel, 1H,I and Table 1). NGF-treated cells also exhibit a higher number of total mitochondria *per* cell at 4–24 h (Fig. 1F) which, together with a reduction in the mean mitochondrial length at 4 h (Fig. 1G) further suggests the increase in mitochondrial fragmentation at early stages of the differentiation. These observations are consistent with our extended [12] hypothesis (and the modeling studies below) that mitochondria do not constitute a homogeneous population with respect to ROS production, damage and thereby engagement in fission or fusion processes. In line with this prediction, our data show that NGF causes the presence of more fragmented mitochondria, while some networked healthy mitochondria are still remaining. With this fission process ongoing, the networked mitochondria would ultimately disappear if not at later stages NGF also increased the ability of mitochondria to fuse with each other (Fig. 1E lower panel, 1H,I and Table 1), as shown by the presence of both fragmented and elongated mitochondria between 20 and 25 h (Fig. 1B,C, white and green arrows, respectively). The increase in networked mitochondria is in agreement with our previous data of Mfn2 induction at 24 h [12]. These changes are suggestive of a very dynamic balance between dispersed and networked mitochondria in NGF-differentiated cells, as evident in the video at 24 h (Video S1-NGF 24 h: 44 s, 1 frame every 0.5 s) and selected frames thereof (Fig. 1D) showing the motility and flowing of mitochondria between dispersed and networked states, in particular in the growth cones and newly formed neurites. Indeed, the time-lapse sequences in Fig. 1B,C show the dynamic behavior of regions rich in dispersed mitochondria (white arrows) toward a mitophagy state, as revealed by the co-localization of mitochondria and lysosomes (orange arrows) in NGF-treated cells, and their disappearance in the following timeframes showing only mitochondria with elongated morphology (green arrows).

Movement of mitochondria and lysosomes along neurites is also evident in Videos S2 and S3. Likewise, the different timing of mitophagy in the perinuclear *versus* the neurite areas is remarkable: the former is limited to early time points, but remains higher than CTR (Figs 1B and 2B upper panel, and 2C), while NGF-induced mitophagy in neurites continues throughout the time-lapse (Figs 1C and 2B lower panel, and 2D). Nonetheless, the total number and volume of mitochondria in NGF-treated cells remains higher than in CTR cells (Fig. 1F and Table 2). This is presumably due to an increased mitochondrial biogenesis. Indeed, MTG staining in the presence of the lysosomal inhibitor Bafilomycin A1 (Baf) (Figs 1H,I and 2A) confirms the impact of NGF on the rates of both mitophagy and mitochondrial biogenesis, as computed in Table 2, according to [36]. This finding is in accordance with the time-dependent increase of Nrf1

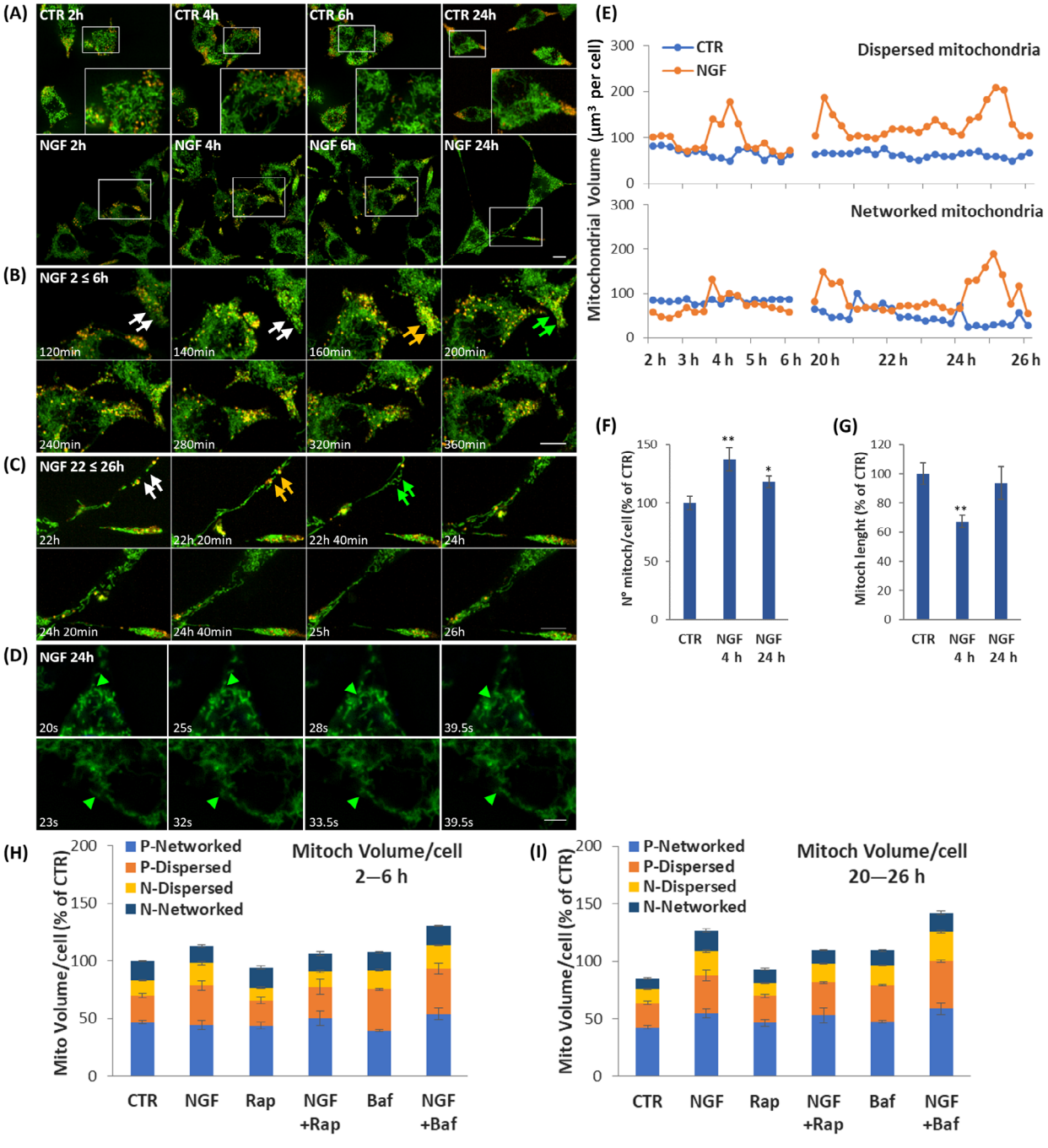

Fig. 1. Analysis of mitochondrial dynamics changes in NGF-treated cells. (A–C) Representative images of MTG-LTR stained PC12 cells in CTR (A), and in 2–6 h (B) or 22–26 h (C) time-lapse imaging after treatment with NGF (10 ng·mL^{-1}). The boxes in (A) represent the enlarged areas of CTR, or regions of selected time-lapse images of NGF-treated cells for 2–6 h (B) or 22–26 h (C). Live imaging was performed by Operetta® CLS on 20 random fields. Regions of fragmented (white arrows) or networked mitochondria (green arrows) and MTG-LTR overlaps (orange arrows) are indicated. Scale bars: 10 μm. (D) Representative frames from live imaging sequences of cells differentiated with NGF for 24 h (Video S1-NGF_24h, 44 s, 1 frame every 0.5 s). The experiment was replicated three times. Green arrowheads indicate the dynamic changes of one mitochondrion in the sequential frames. Scale bar: 5 μm. (E) Volume of fragmented (upper panel) and networked (lower panel) MTG-stained mitochondria at the indicated points of the time-lapse in CTR or NGF-treated cells. Segmentation and quantitation of fragmented/networked mitochondria were performed as described in Methods. Data are the mean of fragmented/networked mitochondria/cell (μm^3 per cell) in about 150 cells of 20 imaged random fields and expressed as a percent of CTR. Similar trends were found in three separate experiments. (F, G) Total number (F) and mean length (G) of MTG-stained mitochondria/cell after NGF treatment for 4 or 24 h. Data, expressed as a percent of CTR ± SEM, are the mean of three experiments with duplicate samples. (H, I) Volume of dispersed and networked mitochondria in the perinuclear (P) and neurite (N) areas in the 2–6 h (H) and 20–26 h (I) time-lapse images of MTG-stained cells treated with NGF (10 ng·mL^{-1}) (images in A–C), and effect of Rap (200 nM) and Baf (100 nM) (images in Fig. 2A). Data, expressed as percent of total mitochondria in the CTR, are the mean ± SEM of perinuclear or neurite fragmented/networked mitochondria/cell in about 150 cells of 20 random fields (values are reported in Table 1). *$P \leq 0.05$, **$P \leq 0.01$ vs the corresponding CTR (ANOVA and Dunnett's multiple comparisons test). Baf, bafilomycin A1; LTR, LysoTracker red; MTG, MitoTracker Green; NGF, Nerve Growth Factor; RAP, rapamycin.

Table 1. Volume of mitochondria/cell. Mean Volume of dispersed and networked mitochondria in the Perinuclear and Neurite regions in the 2–6 h and 20–26 h time-lapse imaging of MTG-stained PC12 cells treated with NGF (10 ng·mL^{-1}) (representative images in Fig. 1A–C), and effect of Rap (200 nM) and Baf (100 nM) (representative images in Fig. 2A). The protocol for mitochondria segmentation and quantitation is detailed in the Methods. Data are the mean of perinuclear and neurite fragmented/networked mitochondria/cell in about 150 cells in 20 random fields and expressed as percent of total mitochondria in the CTR (2–6 h).

	2–6 h					20–26 h				
	Perinuclear networked	Perinuclear dispersed	Neurites dispersed	Neurites networked	Total	Perinuclear networked	Perinuclear dispersed	Neurites dispersed	Neurites networked	Total
CTR	46.6	23.3	13.1	17.0	100.0	42.5	21.3	12.2	9.0	85.0
NGF	44.2	34.2	19.6	15.0	113.0	54.5	33.3	21.3	17.7	126.7
Rap	43.8	21.9	11.0	17.4	94.1	46.5	23.3	11.3	12.0	93.1
NGF + Rap	50.2	27.1	13.6	15.3	106.3	53.0	28.5	16.6	11.7	109.7
Baf	39.5	35.9	16.7	15.5	107.5	47.4	31.8	17.5	12.6	109.2
NGF + Baf	54.1	39.2	20.3	17.1	130.7	58.9	41.5	25.3	16.3	142.0

(Goglia and Colangelo, unpublished), as well as with our previous findings showing that NGF increases mtDNA and levels of Sirt3, mtTFA and PPARγ [12], which are known to modulate mitochondrial biogenesis and metabolism. As mitophagy clears out damaged mitochondria, while association of mitochondria in elongated structures is known to increase their efficiency, our data suggest that NGF may improve mitochondrial quality by activating their biogenesis (as in the modeling below).

Both mitochondrial fission and mitophagy are essential for full neuronal differentiation

To validate the role of mitophagy during NGF differentiation, we assessed the effect of Rapamycin (Rap) and NAD$^+$. We found that the autophagy inducer Rap, which failed to affect PC12 differentiation [12], is *per se* unable to change mitochondrial morphology, while minimally influencing basal and NGF-induced mitophagy (Figs 2 and 1H,I and Table 1), in agreement with similar findings in other cellular systems [36,37]. Instead, NAD$^+$ (known as a mitophagy inducer effective in neuroprotection) [8] causes an early increase of MTG-LTR co-localization (2–6 h) and a strong induction during the 20–24 h time-lapse (Fig. 3A,B), although with minor changes in dispersed mitochondria compared to NGF (Fig. 3C).

Interestingly, we observed that NAD$^+$ is able to accelerate neurite outgrowth in PC12 at 4–24 h, but its differentiating activity is transient and abruptly lost after 24 h (Fig. 3D,E). In fact, NAD$^+$-treated cells do not acquire the typical neuronal morphology induced by NGF, as measured by the cell surface area and sphericity (Fig. 3F,G) and the lower β3-Tubulin and GAP43 expression, compared to NGF-differentiated cells (Fig. 3H–J). Intriguingly, NAD$^+$-treated cells display higher mitochondrial membrane potential, although to

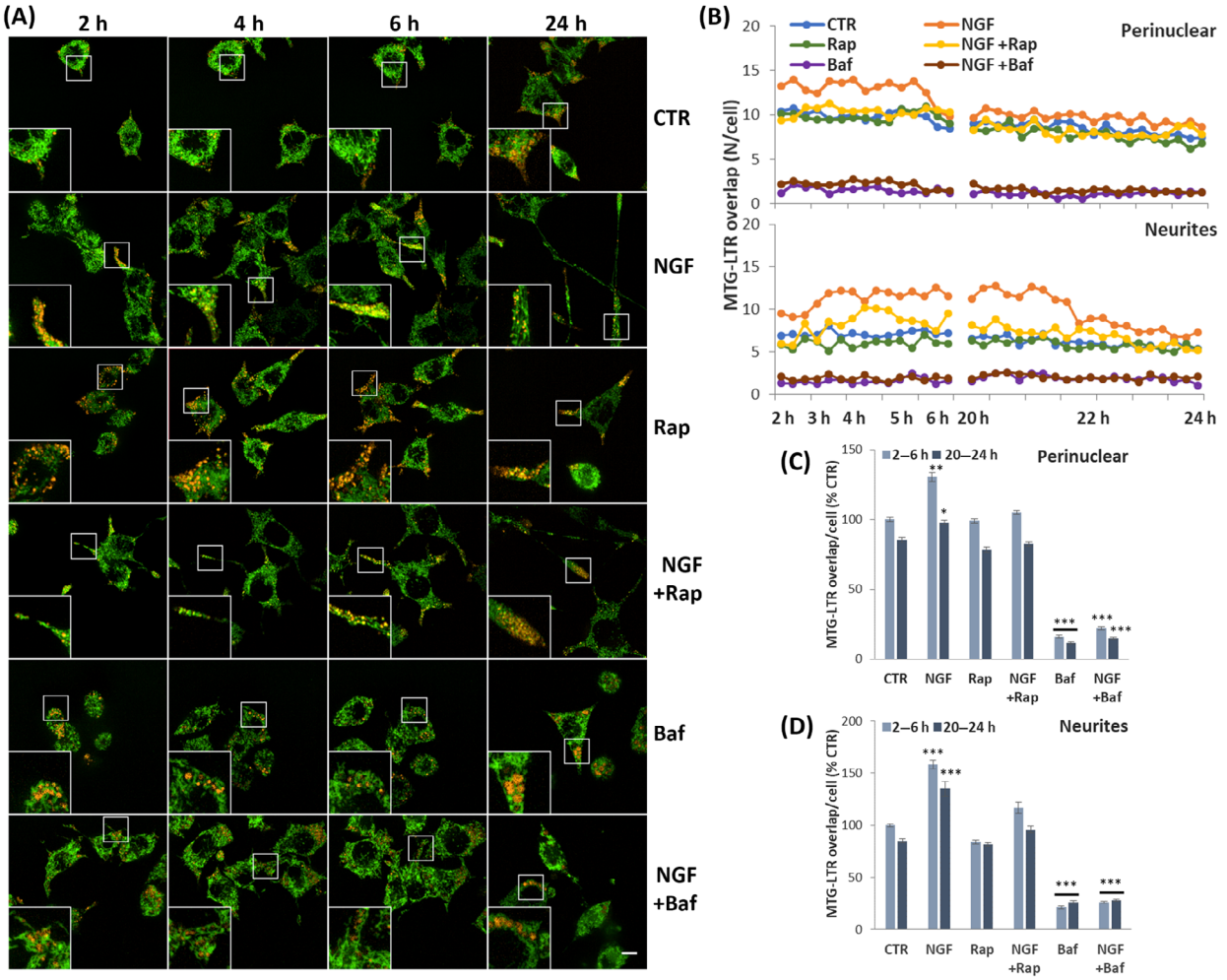

Fig. 2. Mitochondria morphology and mitophagy during NGF differentiation. (A) Representative images of MTG-LTR stained PC12 cells at the indicated times of a 2–6 and 20–26 h time-lapse imaging after treatment with NGF (10 ng·mL^{-1}), and effect of Rap (200 nM) and Baf (100 nM). Live imaging was performed by Operetta® CLS on 20 random fields. Scale bar: 10 μm. (B) MTG-LTR overlapping profiles during the 2–6 and 20–24 h time-lapse imaging in Perinuclear and Neurite areas of NGF-treated cells, and effect of Rap and Baf. Similar profiles were found in three separate experiments. (C, D) Quantitation of MTG-LTR co-localization in the Perinuclear (C) and Neurite (D) regions during the 2–6 and 20–24 h time-lapse imaging of MTG-LTR stained cells exposed to NGF (10 ng·mL^{-1}), and effect of Rap (200 nM) and Baf (100 nM). Data, expressed as a percent of CTR, are the mean ± SEM of overlapping MTG-LTR spots/cell in about 150 cells of 20 random fields in three independent experiments with duplicate samples. *$P \leq 0.05$, **$P \leq 0.01$, ***$P \leq 0.001$ vs the corresponding CTR (ANOVA and Dunnett's multiple comparisons test). Baf, bafilomycin A1; LTR, LysoTracker red; MTG, MitoTracker green; NGF, nerve growth factor; RAP, rapamycin.

a lesser extent compared to NGF (Fig. 4A,C), suggesting that both NGF- and NAD$^+$-induced mitophagy result in improved mitochondrial quality. Nonetheless, NAD$^+$ produces higher ROS levels than NGF at 4 h, and prolonged exposure to NAD$^+$ causes massive accumulation of ROS at 72 h (Fig. 4D) and decreased cell viability, as measured by MTT assay and the number of apoptotic nuclei (Fig. 4B,E,F). Altogether these data showing the opposite effect of Rap and NAD$^+$, further support our hypothesis that both mitochondrial dynamics and mitophagy are needed for differentiation, at least at early stages, while full differentiation requires transcriptional/metabolic programs that are peculiar to NGF signaling, such as Akt pathway-related genes, whose expression is reduced by NAD$^+$ in neural progenitor cells [38].

Construction of the fusion–fission–mitophagy cycling model at the *core* of neuronal differentiation

To further explore the impact that the fission rate enhancement may have on neuronal differentiation, and to examine whether this alone could mediate the

Table 2. Calculation of mitophagy and biogenesis rates. Values of total mitochondrial mass in MTG-stained cells exposed to NGF (10 ng·mL^{-1}), or NGF + Baf (data from Table 1). Values were used to calculate the effect of NGF on mitophagy [computed as the difference in mitochondrial mass between (NGF + Baf) and (NGF alone)] and biogenesis [computed as the difference in mitochondrial mass between (NGF + Baf) and (Baf alone)], according to Mauro-Lizcano *et al.* [36].

	MTG staining	Mitophagy rate	Biogenesis rate
CTR	100.00	7.51	0.00
NGF 4 h	112.97	17.70	23.17
NGF 24 h	126.74	15.22	34.45
Baf	107.51		
NGF + Baf 4 h	130.67		
NGF + Baf 24 h	141.96		

effects of NGF addition, we developed a mathematical model integrating the experimentally observed mitochondrial dynamics, ROS production and mitophagy processes (Fig. 5A and Appendix S1: Computational Modeling). The model includes (a) two types of mitochondria: networked ('*N*') and fragmented (dispersed '*D*') mitochondria in three different states, *i.e.* healthy (*N* and *D*), mildly damaged ('*Nd*' and '*Dd*') and severely damaged ('*Ndd*' and '*Ddd*'); (b) ROS produced by dispersed ('*ROS*') and by networked ('*ros*') mitochondria, which influence the state of mitochondria and cause their transition to more damaged states (*i.e.*, *Dd*→*Ddd*, and *N*□*Nd*□*Ndd*, respectively); (c) the cycling process between networked (*N*) and dispersed (*D*) mitochondria through fission/fusion (Fig. 5A, curved arrows); (d) mitochondrial synthesis, producing networked (*N*) mitochondria; and (e) removal of severely damaged fragmented mitochondria (*Ddd*) by mitophagy [15,16].

We selected these components because the balance of network/dispersed mitochondria is at the *core* of the fusion–fission–mitophagy cycling events. Modification of mitochondrial populations in terms of shape and number reflects their functional properties, as well as the flux of mitochondria-related processes. Instead, ROS production is a hallmark of damaged mitochondria: they are overproduced by impaired mitochondria and produce damage to the healthy ones, therefore used here as a readout of the model validity. ROS are degraded by the reactions "v_{ROSd}" and "v_{rosd}", which are influenced by ROS concentration and by the kinetic constants "k_ROS degradation" and "k_ros degradation". The diagrammatic model of Fig. 5A was translated into a mathematical model in terms of rate and balance equations, and then integrated using Copasi [39]. *N*, *Nd*, *Ndd*, *D*, *Dd*, *Ddd* mitochondria and *ROS*/*ros* are used in the model as single species and expressed in μmol·L^{-1}. Reactions (i.e., cycling between networked and dispersed mitochondria, ROS production and elimination) are modeled as irreversible functions of mass action and are composed of the rate constants (fission or fusion rate constants) and the concentrations of their substrates. Therefore, changes in the rate constants, or in the amounts of substrates, modify the reactions involved in the formation of networked and dispersed mitochondria. Instead, mitophagy is modeled as a Michaelis–Menten function. Mathematical models and more detailed descriptions thereof are provided in the Appendix S1 (Computational Modeling), which includes a Table listing all the mathematical equations. As the model is a network model, a change in any parameter can affect any other dependent variable, directly or indirectly (Modeling scheme in Appendix S1), thus allowing to simulate the effect of any perturbation that is supposed to act through the components of the model. Using this model we were able to simulate how changes in mitochondrial dispersion (*N*□*D*) might help improve mitochondrial quality and decrease ROS levels.

Validation: the model is able to simulate the effect of perturbations involving mitochondrial processes

To test our model in the context of NGF differentiation, we assessed the effect that NGF increasing the fission rate constant should have on ROS formation. Starting from an initial steady state (low basal cycling and mitophagy), our Copasi simulations (Appendix S1: Fusion–fission Model) show that a 20-fold increase in the fission rate constant (from 0.18 to 3.6) should indeed cause a transient increase in ROS by approximately 70% (Fig. 5B,C; Appendix S1: Computational Modeling and related Copasi files). At early stages, it should also reduce (from 60% to 10%) the percentage of mitochondria in networks (Fig. 5B). Indeed, the model is able to reproduce the experimental data: the (a) the transient increase in ROS [Fig. 5B–D (predicted and experimental)]; (b) the transient rise in *Ddd* mitochondria ready to undergo mitophagy (Fig. 5C), as experimentally observed in Fig. 1E (upper panel); (c) the transient increase in mitophagy flux (Fig. 5E), as shown in Fig. 2; (d) the increase in fusion flux (Fig. 5E), corresponding to the rise in elongated mitochondria in Figs 5B and 1E (lower panel) and induction of Mfn2 [12]; and (e) the enhanced quality of mitochondria (active mitochondria in Fig. 5B), as experimentally observed in terms of mitochondrial potential (Fig. 4A,

C) and higher basal respiration [12]. The increase in networked mitochondria (Fig. 5B) validates the mitochondrial cycling proposed by the model: it predicts the higher fusion flux, consequent of the higher fission flux (Fig. 5E and Appendix S1: Computational Modeling). The enhanced mitochondrial quality (active mitochondria

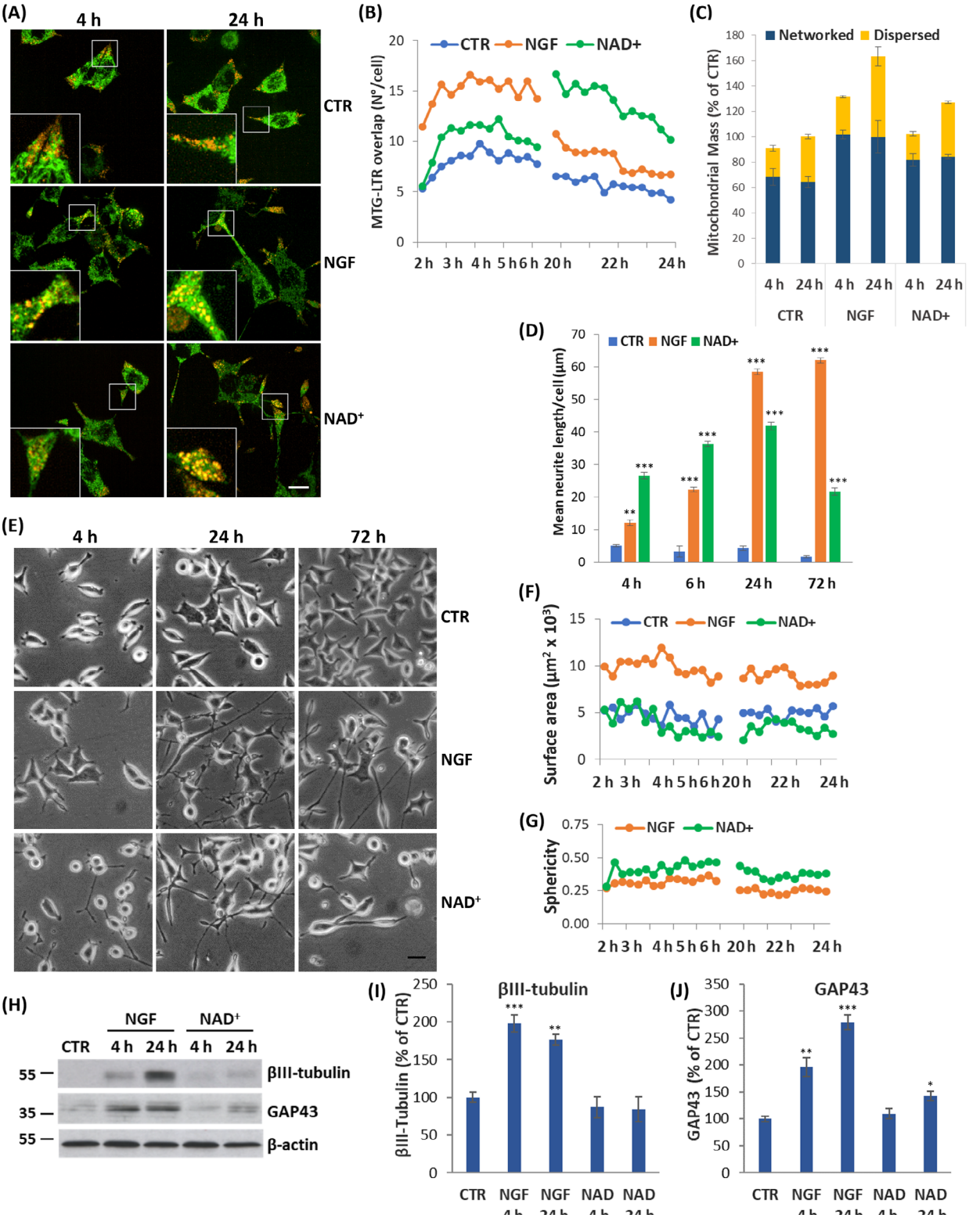

Fig. 3. NAD^+ stimulates mitophagy and transient differentiation. (A) Representative images of MTG-LTR stained PC12 cells at 4 and 24 h of live imaging after treatment with NGF (10 ng·mL^{-1}) or NAD^+ (100 μM). Live imaging was performed by Operetta® CLS ($N = 6$ for each treatment). Scale bar: 10 μm. (B) MTG-LTR overlapping profiles during the 2–6 and 20–24 h time-lapse imaging of NGF- or NAD^+-treated cells. Similar profiles were observed in three separate experiments in duplicate. (C) Volume of MTG-stained mitochondria populations at 4–24 h of the time-lapse on NGF- or NAD^+-treated cells. Data, expressed as a percent of CTR, are the mean ± SEM of fragmented/networked mitochondria/cell in about 150 cells of 20 random fields ($N = 6$). (D) PC12 differentiation measured as average neurite length per cell (μm). Data are the mean ± SEM of six independent samples. (E) Representative images of cells exposed to NGF or NAD^+ for 4–24–72 h. Scale bar: 25 μm. (F, G) Measurement of Surface area (F) and Sphericity (G) in cells treated with NGF or NAD^+ during a time-lapse (2–6 and 20–26 h) imaging in bright-field by Operetta® CLS. 3D analysis was performed using Harmony software as described in the Methods. Data are the mean values (about 150 cells in 20 imaged random fields) of three separate experiments in duplicate. (H–J) Representative immunoblots (H) and quantitation of βIII-Tubulin (I) and GAP43 (J) in lysates from PC12 treated with NGF or NAD^+ for 4–24 h. Data, expressed as a percent of CTR ± SEM, are the mean of two experiments with duplicate samples ($N = 4$). *$P \leq 0.05$, **$P \leq 0.01$, ***$P \leq 0.001$ vs CTR (ANOVA and Dunnett's multiple comparisons test). GAP43, growth associated protein 43; LTR, LysoTracker red; MTG, MitoTracker Green; NAD^+, nicotinamide adenine dinucleotide; NGF, nerve growth factor.

in Fig. 5B) reflects the higher mitophagy flux at early time points (Fig. 5E), due to the increase in mitophagy substrates (*Ddd* mitochondria) (Fig. 5C) caused by the stimulated fission, in agreement with the experimental data (Figs 1 and 2).

Damaged mitochondria should undergo faster fission than their healthier counterparts. However, additional simulations (Appendix S1: Computational Modeling and related Copasi model-bis) show that both the model behavior and the fitting of ROS with the experimental data do not change significantly when applying different fission rate constants for the distinct types of mitochondria, compared to the model in Fig. 5. These results denote the robustness of our model. This means that the model is able to simulate the experimental data. It further confirms that NGF may stimulate differentiation by increasing fission.

Our experimental data suggest that the ability of NGF to modulate mitochondrial fission and thereby mitophagy and mitochondrial quality might be essential for ROS homeostasis and differentiation. To assess this hypothesis on our model, we performed additional Copasi simulations with lower induction of fission (Appendix S1: Computational modeling). Indeed, we found that a lower increase in the fission rate constant (from 0 to 0.36, or 0.9, or 1.8, instead of 3.6 as it is in the model) induces smaller variations of the mitophagy (Fig. 5F), which is inversely correlated to ROS accumulation. In fact, the simulations of the impact of mitophagy on ROS show that a decrease in the mitophagy flux [by reducing the mitophagy rate constant ($k_M = 1 \times 10^{-4}$ or 1×10^{-5}, instead of 4×10^{-4} as it is in the model)] produces a permanent rise in ROS levels after 6 h (Fig. 5G), thus reproducing the effect of Baf inhibition on NGF activity [12]. Instead, the peak of ROS is lowered when the rate constant of mitophagy is further increased to k_M 1×10^{-2} (Fig. 5G). These simulations show that perturbations altering fission and thereby mitophagy can control ROS accumulation, as well as fractions of networked/-dispersed and active mitochondria.

To further assess the impact of mitophagy on mitochondrial quality, we modeled an increase of the rate constant k_M of the mitophagy reaction (from 0.0004 to 0.002). Interestingly, the simulation of 'high mitophagy flux' together with increased fission (Fig. 5H, solid lines) causes an increase of the ratio Active mitochondria/Total mitochondria, compared to the condition with fission modulation alone (Fig. 5H, dotted lines). Altogether, the computational model and the simulations are able to reproduce all the experimental data, thus providing a valid computational tool for the interpretation of the experimental data and for future studies aiming to further detail the activity of NGF on mitochondrial processes.

NGF induction of mitochondrial dynamics and mitophagy is regulated by PI3K/Akt and JNK signaling

We next assessed the NGF differentiation signaling in the context of mitochondrial dynamics and mitophagy, both the PI3K/Akt signaling regulating survival and Rac-mediated neurite outgrowth [40], and the c-Jun N-terminal kinase (JNK-1) signaling known to stimulate ROS production and neuritogenesis [31,32,41,42]. Indeed, we observed that NGF-mediated differentiation induces P-JNK and is prevented by its pharmacological inhibition (Fig. 6A–C). Remarkably, NGF-induced mitophagy (overlap of MTG-LTR) is significantly prevented by both wortmannin (WT) and JNK inhibition (JNKi) (Fig. 6D,E). Furthermore, WT abolishes the NGF-mediated reduction of the mean mitochondrial length (Fig. 6F), thus implying a role for PI3K in modulating both fission and mitophagy. Instead, JNKi produces an overall reduction of the mitochondrial length

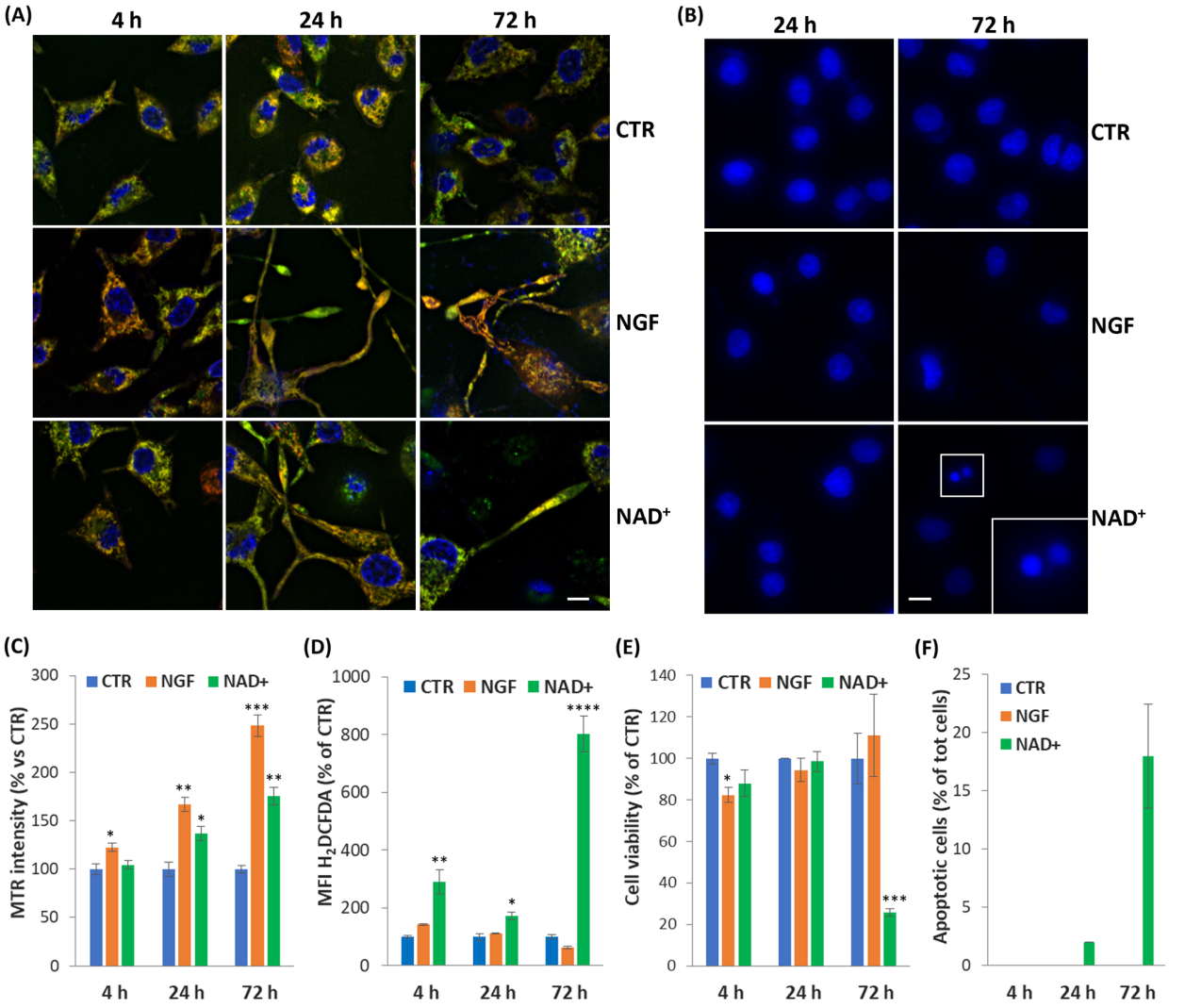

Fig. 4. Prolonged exposure to NAD^+ causes cell death. (A) Representative images of MTR/MTG-stained cells treated with NGF (10 ng·mL^{-1}) or NAD^+ (100 μM) for 4–24–72 h. Live imaging was performed by the THUNDER Imager Live Cell LEICA on about 100 cells in 15 random fields. Scale bar: 10 μm. (B) Representative images of Hoechst-33342 staining of apoptotic nuclei in PC12 cells treated with NGF or NAD^+ for 24–72 h. Magnification 40×. Scale bar: 10 μm. (C) Quantitation of MTR mean fluorescence intensity in MTR-stained cells treated with NGF or NAD^+ for 4–24–72 h. Data, expressed as percent of total cells in 10 random fields for each sample, are the mean ± SEM of three independent experiments with duplicate samples. (D) Quantitation of ROS levels by H_2DCFDA staining of cells treated with NGF or NAD^+ for 4–24–72 h. Data, expressed as percent of CTR, are the mean ± SEM of three independent experiments in duplicate ($N = 6$). (E) Cell viability by MTT assay of cells treated with NGF or NAD^+ for 4–24–72 h. Data, expressed as percent of CTR, are the mean ± SEM of two separate experiments, each with five samples. (F) Quantitation of apoptotic nuclei after exposure to NGF or NAD^+ for 4–24–72 h. Data are the mean ± SEM of five independent samples. *$P \leq 0.05$, **$P \leq 0.01$, ***$P \leq 0.001$, ****$P \leq 0.0001$ *vs* CTR (ANOVA and Dunnett's multiple comparisons test). H_2DCF-DA, dichloro-dihydrofluoresceine diacetate; MTG, MitoTracker Green; MTR, MitoTracker Red CMXRos; NAD^+, nicotinamide adenine dinucleotide; NGF, nerve growth factor; ROS, reactive oxygen species.

(Fig. 6F), suggesting a role of JNK in modulating mitophagy only, but not NGF-induced fission, thus leading to accumulation of fragmented mitochondria. The effect of JNKi is similar to that of Compound C (CC), a specific inhibitor of the free-energy sensor AMPK, which fully abolishes NGF-induced mitophagy (Fig. 6D,E), thus causing accumulation of fragmented mitochondria (Fig. 6F). Since CC completely blocks NGF-induced differentiation (Fig. 6A), as previously reported [12], these data further support our concept that both mitochondrial dynamics and mitophagy are needed for the differentiation and that NGF stimulates mechanisms boosting energy metabolism, thereby activating fission and mitophagy.

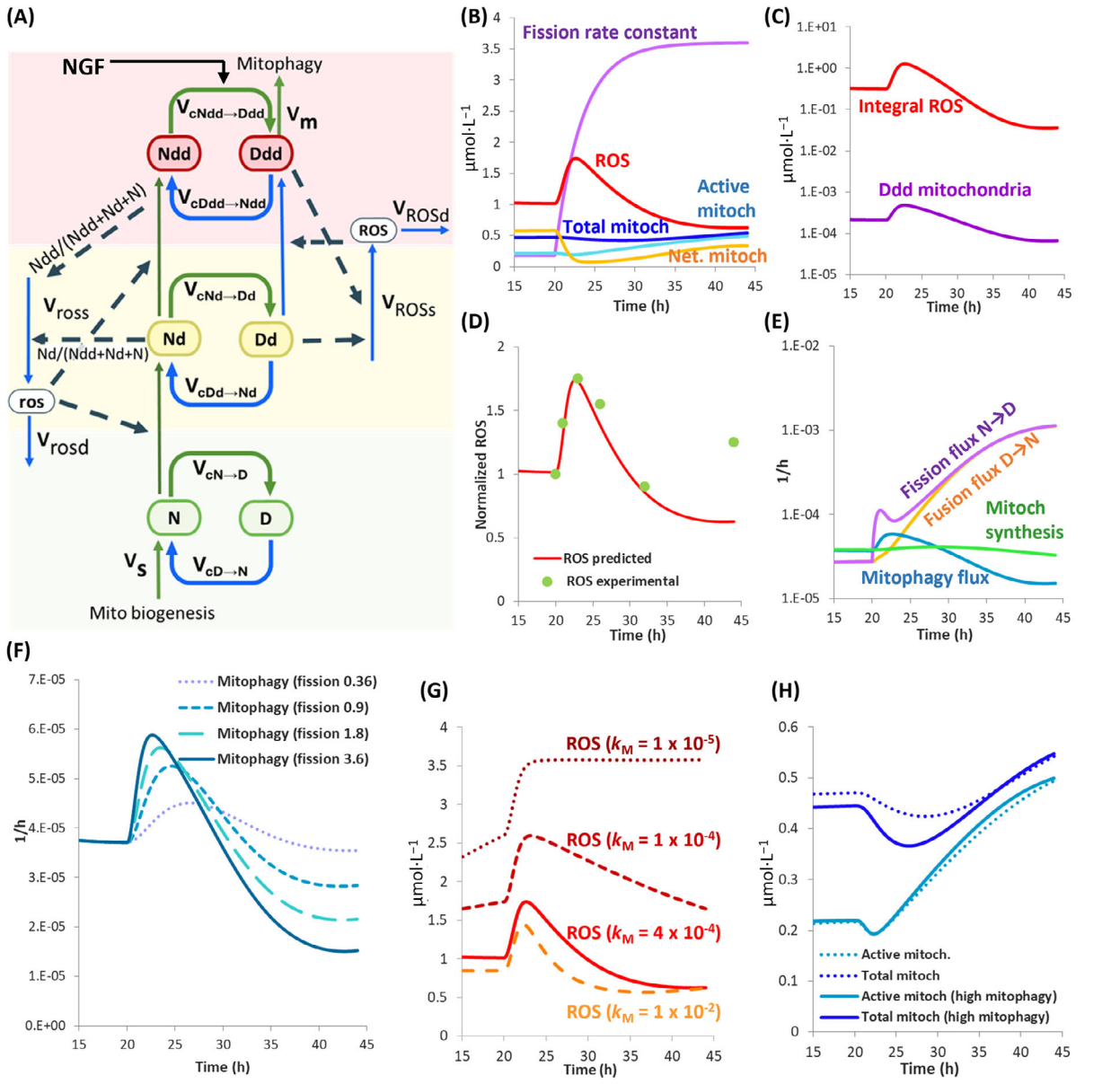

Fig. 5. The fusion–fission–mitophagy cycling model at neuronal differentiation. (A) Proposed model of networked (N) and dispersed (D) mitochondria and cycling between fission and fusion (curved arrows). 'd' and 'dd' refer to mildly and highly damaged mitochondria, respectively; 'ROS' and 'ros' refer to ROS near damaged D and N mitochondria, respectively. Solid arrows refer to conversions, while dashed arrows refer to regulation; 'v' refers to reaction rates. (B, C) Modeling NGF-induced differentiation by increasing the fission rate constant and model response in terms of (B) ROS content, total mitochondria, active mitochondria, and networked mitochondria; (C) Integral ROS and Ddd mitochondria. (D) Fit of the model (line) to experimental (dots) data of ROS induced by NGF. Copasi simulations are based on experimental data from [12] (Copasi Fig 5.cps). (E) Modeling the effect of increasing the fission rate constant on fission, fusion, mitophagy flux, and mitochondrial synthesis. (F) Copasi simulation showing the changes in the mitophagy flux when increasing the fission rate constant to 0.36, 0.9, 1.8, or 3.6. (G) Copasi simulation showing the changes in ROS levels upon reducing (1×10^{-4} and 1×10^{-5}) or increasing (1×10^{-2}) the k_M of the mitophagy flux. (H) Modeling the effect of high mitophagy on total and active mitochondria. The decrease in total mitochondria produces a higher mitochondrial quality computed as an increase in the ratio of Total/Active mitochondria. In all Copasi, the system was allowed to reach a steady state between time 0–20 h (T_0 = 20 h). D, healthy dispersed mitochondria; Dd, mildly damaged dispersed mitochondria; Ddd, severely damaged dispersed mitochondria; Mitoch, mitochondria; N, healthy networked mitochondria; Nd, mildly damaged networked mitochondria; Ndd, severely damaged networked mitochondria; ROS, Reactive Oxygen Species; V_m, Mitophagy (reaction); V_{ROSd}, degradation of ROS produced by Dd and Ddd (reaction); V_{rosd}, degradation of ROS produced by Nd and Ndd (reaction); V_{ROSs}, ROS synthesis by Dd and Ddd (reaction); V_{ross}, ROS synthesis by Nd and Ndd (reaction); V_s, mitochondria biogenesis (reaction).

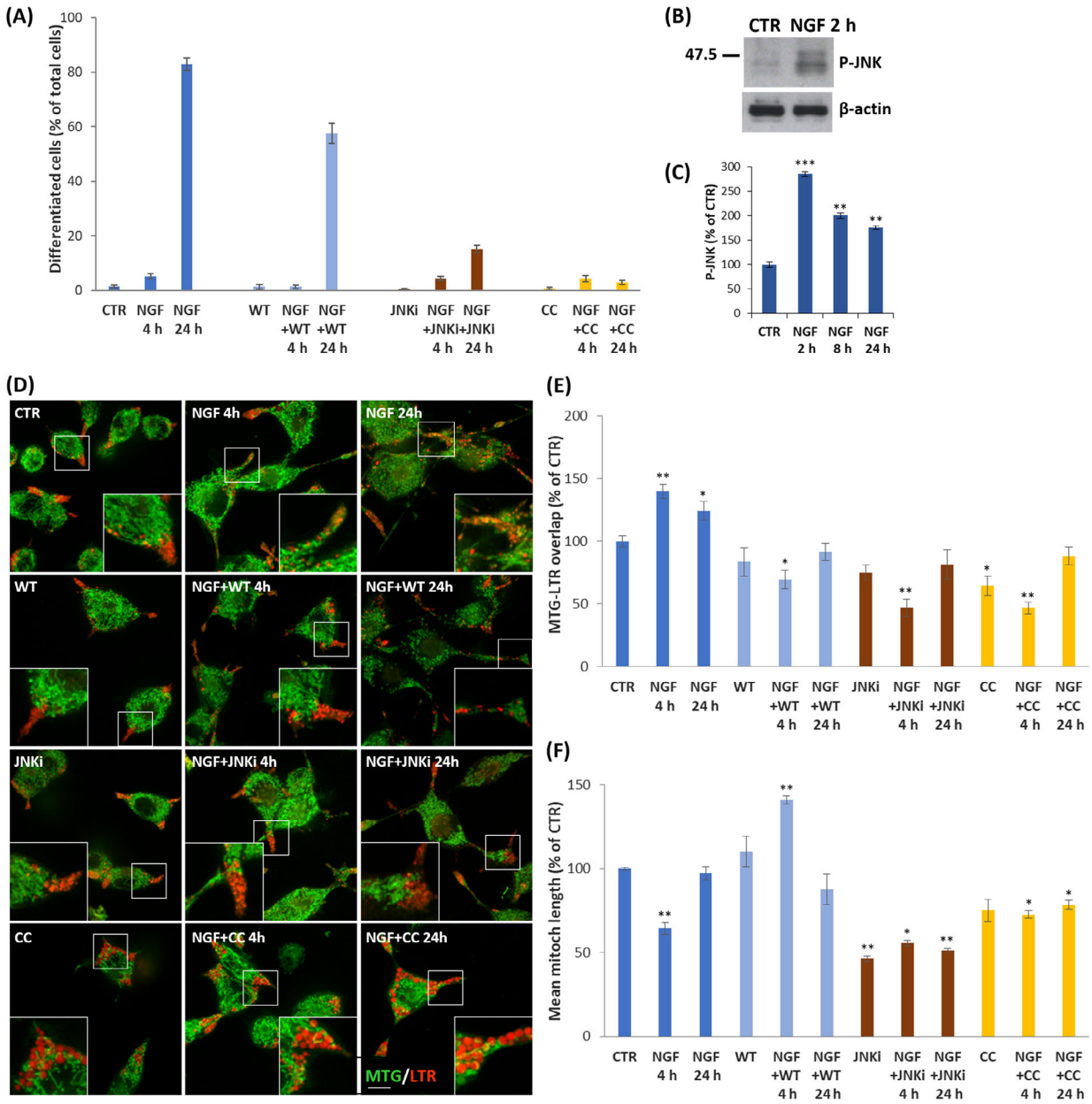

Fig. 6. Impact of PI3K and JNK signaling on mitochondria morphology and mitophagy during NGF differentiation. (A) Effect of PI3K inhibitor wortmannin (WT), the JNK inhibitor II (SP600125), or the AMPK inhibitor Compound C (CC) on NGF-induced differentiation. Data are the mean ± SEM of six independent samples. (B, C) Representative immunoblot (B) of P-JNK in PC12 cells treated with NGF for 2 h, and quantitation (C) of P-JNK/JNK ratio after 2–8–24 h, normalized by the β-Actin content. Data are the mean ± SEM of two experiments with two independent samples. (D) Representative images of MTG-LTR-stained PC12 cells treated with NGF (10 ng·mL^{-1}) for 4 or 24 h, and the effect of preincubation (10 min) with WT, JNKi, or CC. Live imaging was performed by Operetta® CLS (63×) and quantitation of MTG-stained fragmented/networked mitochondria, and of MTG-LTR co-localization, was achieved using the segmentation protocol described in the Methods section. Images are from three independent experiments with duplicate samples. Scale bar: 10 μm. (E, F) Quantitation of MTG-LTR overlapping (E) and of the mean mitochondrial length (F) in about 150 cells in 20 random fields in three separate experiments with two independent samples. *$P \leq 0.05$, **$P \leq 0.01$, ***$P \leq 0.001$ vs the corresponding CTR (ANOVA and Dunnett's multiple comparisons test). Cc, AMPK inhibitor compound C; JNKi, c-Jun N-terminal kinase inhibitor; LTR, LysoTracker red; MTG, MitoTracker Green; NGF, nerve growth factor; PI3K, phosphoinositol-3-kinase; WT, wortmannin (PI3K inhibitor).

NGF regulates the expression of proteins controlling the quality of mitochondria

The quality control of mitochondria relies on a large number of signaling pathways and mechanisms, including mitochondrial dynamics and mitophagy [18,22]. To further investigate the impact of NGF on mitochondrial quality, we assessed the expression levels of proteins regulating mitochondrial function and homeostasis, with the increased mitochondrial membrane potential observed in Fig. 4A,C as background. Parkin tends to be recruited to depolarized mitochondria [18]. Indeed, immunoblot of total lysates showed that NGF increases Parkin levels (Fig. 7E,G) as well as Parkin-Ambra1 interaction (Fig. 7D,F) thereby probably effecting the removal of exhausted mitochondria by mitophagy [18], despite the increase of TOMM20, a translocase of the outer mitochondrial membrane (Fig. 7A,C,E,I). In addition, we evaluated the functional role of NGF in modulating mitochondrial integrity and cell viability, as substantiated by the increase in Bcl-xL (Fig. 7E,K), which controls the permeability of the mitochondrial membrane, as well as by the higher levels of SOD1 (Fig. 7E,L) and of the ROS sensor DJ-1, which shows increased mitochondrial (Fig. 7A,B) and nuclear localization (Fig. 7A,B,J,M). Instead, we found that NGF minimally affects levels of the mitochondrial protease Omi-HtrA2 (Fig. 7A,C), as confirmed by immunoblot (Fig. 7E,H). Remarkably, however, Omi-HtrA2 retains a prevalent mitochondrial localization, after a transient decrease at 4 h (Fig. 7A,C), in agreement with its crucial function in maintaining the correct balance of Opa1 isoforms (short and long) inside mitochondria, thus contributing to the fission/fusion balance [24]. Altogether, these data integrate our previous observations that NGF modulates fission/fusion (P-Drp1, Mfn2 and Opa1), biogenesis and autophagy (Ambra1) proteins through the activation of AMPK and Ca^{2+}-CaMK signaling [12] to favor mitochondria quality and distribution along neurites while complying with higher energy supply for the differentiation [12].

NGF boosts energy metabolism and redox homeostasis

Mitochondrial dynamics is connected with metabolic rewiring during brain development [1,9]. We have previously shown that NGF differentiation stimulates mitochondrial respiration, but reduces ATP levels at early stages [12]. To further assess the impact of NGF on mitochondrial function and metabolism, we performed untargeted metabolomics on PC12 cells exposed to NGF for 4 or 24 h. As shown in Fig. 8A, the metabolic profiling identifies 46 metabolites with statistically significant changes. Specifically, NGF-treated cells display a significant increase in Glucose (Glc) metabolism, which preferentially enters the Tricarboxylic acid (TCA) cycle, as inferred by the average two-fold higher content in both pyruvate (Pyr) and TCA cycle metabolites, including citrate/isocitrate (Cit/Isocit), α-ketoglutarate (AKG), succinate (Succ), fumarate (Fum), malate (Mal) and oxaloacetate (OAA) at 4 and 24 h (Fig. 8B,D,E), while lactate (Lac) increases only 1.5 fold at 24 h (Fig. 8C).

Remarkably, the use of TCA cycle for energy metabolism should allow to convey a significant amount of glucose toward the pentose phosphate pathway (PPP) in particular at 4 h, as reflected by the strong increase in the nucleotides precursor D-Ribulose 5-phosphate (R5P) (Fig. 8F), and other PPP intermediates (Fig. 8A). The oxidative phase of PPP should provide reduced nicotinamide adenine dinucleotide phosphate (NADPH) essential for redox homeostasis and anabolic reactions. Other biosynthetic processes induced by NGF may sustain the 1C-metabolism essential for the synthesis of purines and thymidine (Fig. 8A), as well as aminoacid synthesis which produces a net increase in serine (Ser) (Fig. 8G), methionine (Met) (Fig. 8A), cysteine (Cys) and glycine (Gly) (Fig. 8H), and glutamate (Glu)/glutamine (Gln) (Fig. 8J).

Altogether, these metabolic routes are connected to anabolic processes and production of NADPH, as well as to the increase in glutathione (GSH) precursors, i.e. Glu, Cys, Gly and γ-glutamylcysteine (γGC) (Fig. 8A, H–J), leading to enhanced GSH content and subsequently to a higher reduced/oxidized GSH ratio (GSH/GSSG), as compared to CTR (Fig. 8K–M). The higher Glu/Gln metabolism may also help to refill the TCA cycle, thereby fostering the malate–aspartate shuttle to translocate reducing equivalents (NADH) from cytosol to mitochondria for the oxidative phosphorylation.

Interestingly, NGF-induced differentiation also occurs with a significant increase in the hexosamine biosynthetic pathway, as indicated by the higher content in uridine diphosphate N-acetylglucosamine (UDP-GlcNAc) (Fig. 8A). UDP-GlcNAc is used in O-GlcNAcylation, a posttranslational modification in the biosynthesis of glycoproteins and for the regulation of many cellular processes, including gene expression, signal transduction and autophagosome maturation [43], as well as neuronal function by modifying synaptic proteins, such as synapsin I, CaMKII/IV and CREB [44,45].

Overall, the metabolic signature of NGF-differentiated cells is a remarkable increase in Gibbs energy metabolic capacity, anabolic changes and ability

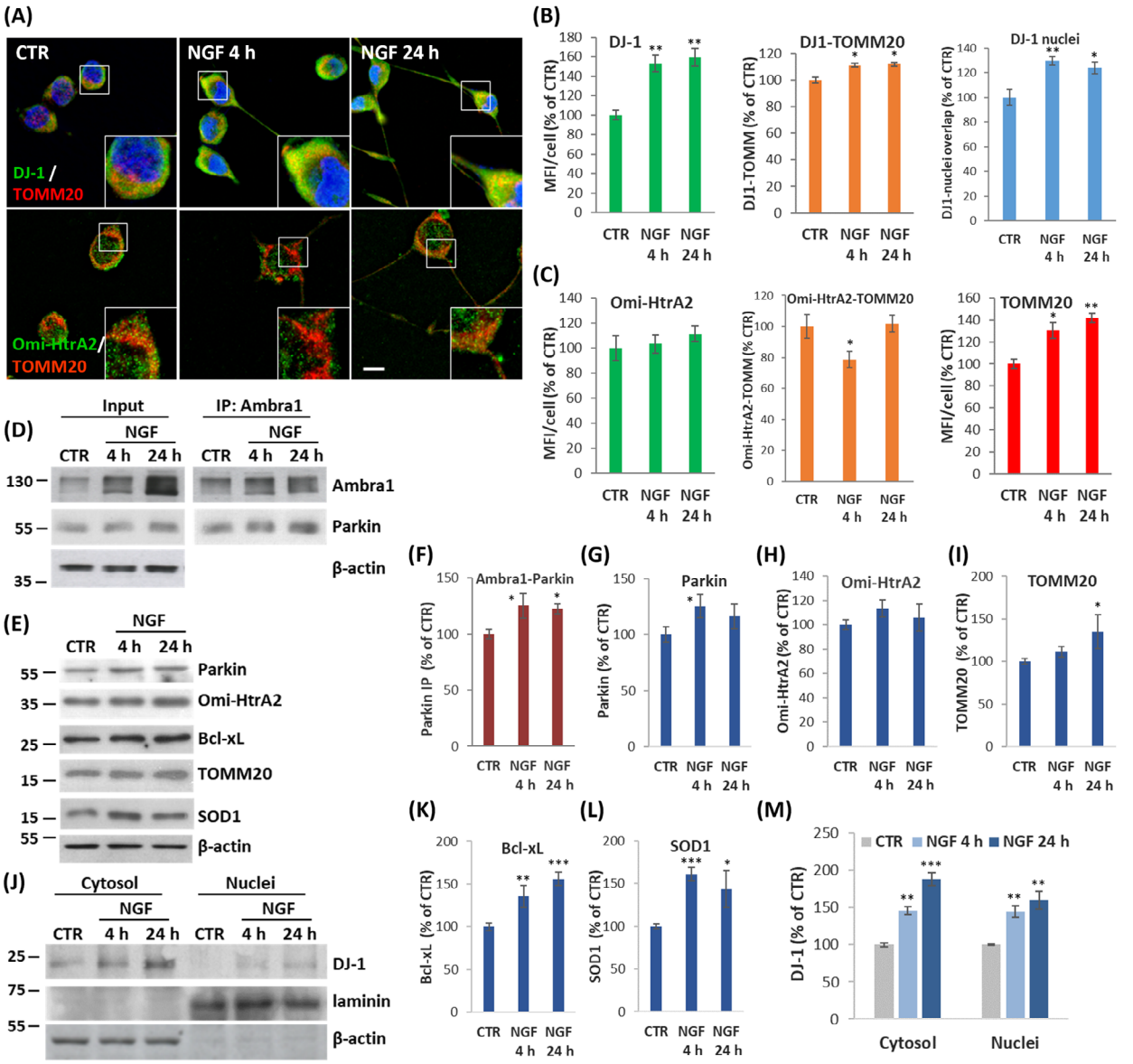

Fig. 7. NGF increases levels of proteins regulating mitochondria homeostasis. (A) Representative merge images of immunostaining for DJ-1 or Omi-HtrA2 in PC12 cells treated with NGF for 4 or 24 h ($N = 4$ for each treatment). Scale bar: 15 μm. (B) Quantitation of the mean fluorescence intensity (MFI) and overlap of DJ-1 with TOMM20 and Hoechst-33 342 (as for the yellow merge in the cytosol and the white/light blue overlap in the nuclei, respectively (images in A). (C) MFI of Omi-HtrA2 and TOMM20 staining and overlap signal (images in A). Data in 'B, C', expressed as a percent of CTR, are the mean ± SEM of two independent experiments with duplicate samples ($N = 4$). (D) Co-immunoprecipitation of Ambra1-Parkin from lysates prepared from PC12 treated with NGF for 4 or 24 h and its quantitation (F) ($N = 4$). (E, J) Representative immunoblot of lysates prepared from PC12 treated with NGF (10 ng·mL^{-1}) for 4 or 24 h ($N = 4$) and assessed for the content of Parkin (E and G), Omi-HtrA2 (E and H), TOMM20 (E and I), Bcl-xL (E and K), SOD1 (E and L) and cytosol/nuclear DJ-1 (J and M). Data (E-M), normalized by the Actin content, are the mean ± SEM of two independent experiments with duplicate samples normalized by the Actin levels. $*P \leq 0.05$, $**P \leq 0.01$, $***P \leq 0.001$ vs CTR (ANOVA and Dunnett's multiple comparisons test). Bcl-xL, BCL2-like 1; NGF, nerve growth factor; SOD1, superoxide dismutase 1; TOMM20, translocase of outer mitochondrial membrane 20.

to sustain the GSH/GSSG redox balance. Interestingly, however, the concomitant increase of lactate, together with TCA intermediates, is suggestive of a certain degree of metabolic "plasticity" of the developing neurons. In fact, reduced glucose (5 mM, instead of 25 mM), or addition of the H^+-ATPase inhibitor Oligomycin A (Olig, 1 μM), and of the electron transport chain inhibitors [i.e. the complex I inhibitor rotenone (Rot, 50 nM) and the complex III inhibitor antimycin A (AA, 0.5 μM)], all reduce neurites outgrowth (Fig. 9A,B).

However, NGF-induced differentiation is fully prevented only when cells are exposed to low glucose (LG) in the presence of OXPHOS inhibitors (Fig. 9A,B), a condition that produces a complete loss of both mitochondrial morphology and transmembrane electric potential (Fig. 9C,D). Our interpretation of the finding that both lactate and TCA cycle intermediates are increased after NGF treatment, is that NGF-mediated rise in glucose transport (Fig. 8E) increases the level of pyruvate (Fig. 8B) and thereby both the anaplerotic reactions (and thereby the levels of TCA cycle intermediates; Fig. 8B,D) and the lactate dehydrogenase (LDH) reaction (i.e. lactate; Fig. 8C). In fact, NGF differentiation only produces a modest reduction of the LDH-A (the M isoform converting pyruvate to lactate), which is significantly reduced only after 12 days of NGF treatment [46]. The NGF effect on the activation of glucose transport is further substantiated by the increase in levels of metabolites of the pentose phosphate pathway (Fig. 8F). Altogether, our data indicate that, while inducing neuronal differentiation, NGF also drives a remarkable reprogramming of metabolic functions: NGF boosts energy metabolism through the TCA cycle and oxidative phosphorylation, presumably to comply with the high energy demand imposed by the neuronal phenotype, thus substantiating our initial hypothesis. At the same time, NGF fosters the PPP cycle and all the anabolic processes to provide building blocks for morphological remodeling, and Glu/Gln metabolism for the synthesis of GSH, which is a major neuronal ROS scavenger system.

Discussion

Development of the neuronal phenotype occurs with the coordination of complex processes downstream of signaling pathways, gene expression and posttranslational modifications, thereby promoting substantial morphological, biochemical and metabolic adaptations to the new functions, while ensuring the maintenance of homeostasis within the brain parenchyma [47]. In neuronal differentiation, individual mitochondria are needed to populate the emerging axons and to travel down their length. We therefore examined NGF-mediated differentiation in some detail both in an earlier paper [12] and again in this study where we added live imaging analysis of mitochondria and mitophagy (Figs 1–3) and their connection with the metabolic reprogramming (Figs 8 and 9).

To deal with the complexity of the mitochondrial dynamics, we also constructed a network scheme (Fig. 5A) and a mathematical model thereof. Our fusion–fission–mitophagy model predicted successfully the experimental observations of changes in respiration and ROS levels upon NGF addition [12], as well as the cycling between elongated and fragmented mitochondria and the degradation of the dispersed damaged mitochondria by mitophagy (Figs 1–3 and Videos S1–S3). This is a strength of the present work: Now there is a validated quantitative elaboration of the fusion–fission–mitophagy model (Fig. 5A), which can help understand the roles played by fusion–fission–mitophagy in mitochondrial quality control. In this elaboration, NGF increases the fission rate constant to activate fission, thereby increasing the level of dispersed mitochondria, including their ROS-damaged subpopulation, and stimulating mitophagy. We also showed by computation that the proposed integration of these processes could function both to increase the average quality of mitochondria and to provide a mechanism of neuron differentiation where dispersed rather than networked mitochondria are important. This could be for micro-anatomical reasons such as neurite formation, or where generation of ROS due to increased pO2 (in turn due to an increased surface/volume ratio) challenges cell functions. The proposed network mechanism could serve to promote mitophagy with the likely effect of reducing cytochrome c release and apoptosis; it could embody the mitoptosis, i.e. the mitophagy of a dispersed fraction rich in damaged mitochondria, proposed by [48,49]. Thus, mitochondrial cycling may well be instrumental in neuronal differentiation, while enabling mitochondrial quality control (ROS levels were increased, but only transiently), and ultimately enhancing mitochondrial respiration and paradoxically increasing mitochondrial concentration. Through mitophagy, cell viability and mitochondrial quality increased, suggesting that mitoptosis was operational. Tissues with low cell turnover, such as the brain, should be served most with such a mitoptotic escape from cell damage.

That it was possible to capture early stages of NGF-induced differentiation in a mathematical model is paradoxical: On the one hand, neural differentiation is a biochemical process, and all biochemical process should ultimately be computable in terms of chemical rate equations. On the other hand, neuronal differentiation is highly complex, and the mathematical model presented here lacks important aspects thereof, including the transcription regulation of mitophagy and of lysosomal degradation. The values of the kinetic parameters of the model could not be based on direct *in vitro* experiments, in part because the *in vitro* conditions that could mimic the intracellular state of differentiation are incompletely known, and in part because the spatial/nano-anatomical aspects would be missing.

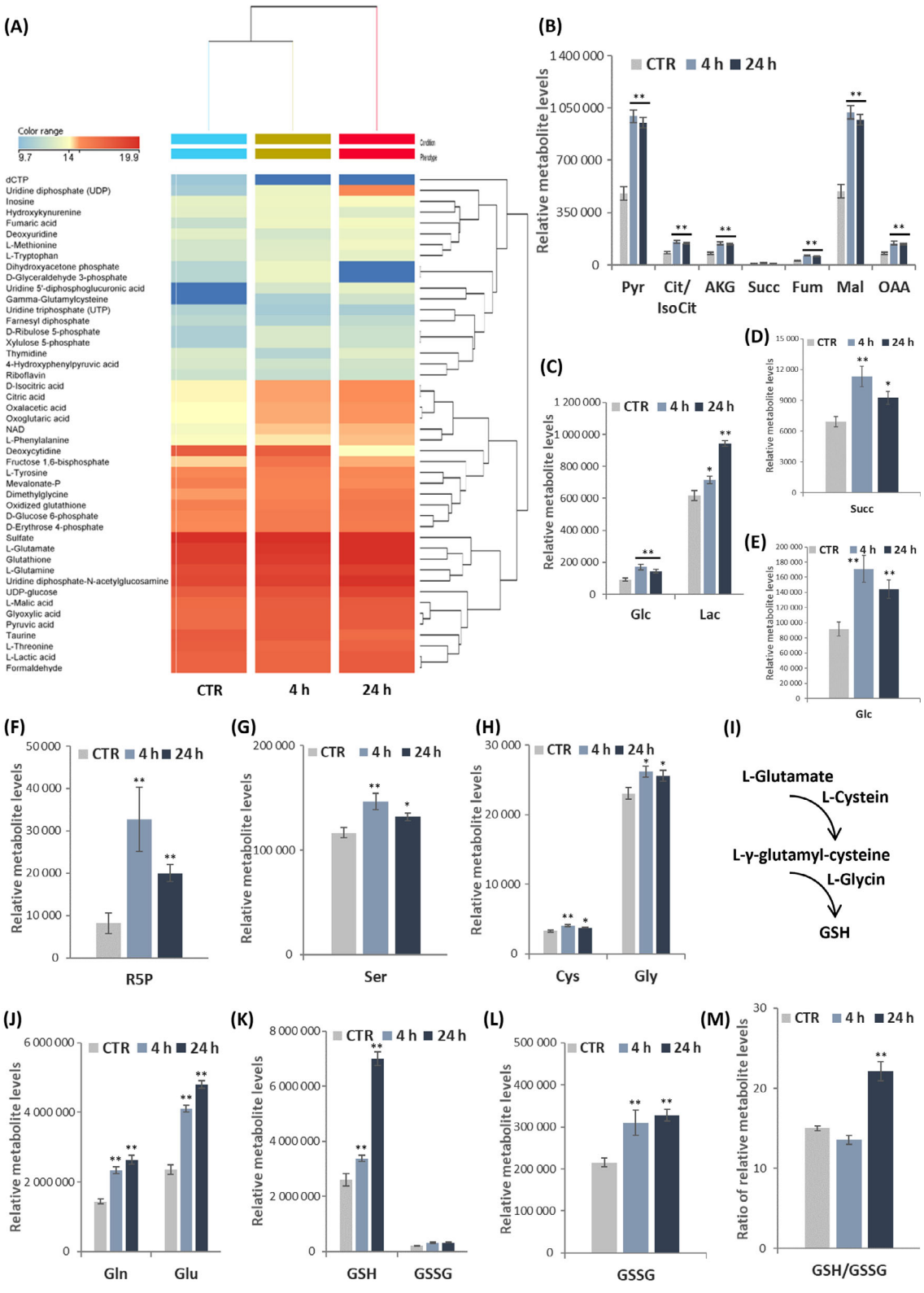

Fig. 8. Untargeted metabolic profiling of NGF-differentiated cells. (A) Hierarchical clustering heatmaps showing significantly different intracellular metabolites by LC–MS in PC12 treated with NGF for 4 or 24 h (Color scale: from blue to red). Metabolic profiles were obtained from six separate samples (each with three technical replicates). (B–M) Relative metabolites abundance of TCA cycle (B and D) glycolysis (C and E), PPP (F) pathways, 1C metabolism (G), Gln-Glu and GSH (H–M). Data are the mean ± SEM of six independent samples in triplicate normalized by the number of total cells in the sample. $*P \leq 0.05$, $**P \leq 0.005$, vs their respective CTR (ANOVA and Dunnett's multiple comparisons test). Cys, cystein; Glc, glucose; Gln, glutamine; Glu, glutamate; Gly, glycine; GSH, reduced glutathione; GSSG, oxidized Glutathione; LC–MS, liquid chromatography-mass spectrometry; NGF, nerve growth factor; PPP, pentose phosphate pathway; R5P, ribose-5-phosphate; Ser, serine; TCA cycle, tricarboxylic acid cycle.

We dealt with the lack of molecular information by (a) using parameter values that are comparable to known parameter values of similar cases, (b) fitting the parameter values to the phenomena that were being modeled, and (c) limiting the complexity of the model [e.g. using the same fission rate constant for the various types of mitochondria (N and Dd)]. The higher fission rate of damaged mitochondria was hereby modeled as due to mass action effects only.

Although the mathematical model fits the experimental data, it cannot yet be considered complete. As always with mathematical models in Biology, future, more targeted experiments should enable us to make the model more realistic at various such points. The availability of the model in the context of quantitative experiments should help this process of model improvement. An advantage of having the model is that one can readily modify the model to add any better information available. We have simulated this for the fission constant. As shown in the Appendix S1, quite an appreciable differentiation between the three fission rate constants affects the simulated curves, but not to the extent that the fit of the experimental data became significantly better.

The mathematical model developed here increases the impact of the experiments that led to its formulation and tests: the model should have a wider applicability than the particular experiment that were used to formulate it. For instance, the model should also address cases of neural differentiation where the same molecules are modulated by medicinal drugs, such as in the management of neurodegenerative pathologies. Because in such cases other molecules may also be present, care should be practiced by carrying out additional experimental tests. The same model can then be used as a starting point for further fine-tuning. Ultimately such fine-tuning should benefit personalized medicine, while such personalized medicine should also help increase the quality of the models.

Remarkably, we also provide new evidence of the complex signaling underlying mitochondrial dynamics during NGF-induced differentiation. Changes in mitochondrial morphology and mitophagy are triggered by a complex interplay between (a) the NGF-PI3K signaling in differentiation/survival, (b) ROS and the stress kinase JNK and (c) the energy sensor AMPK associated to the energy stress due to increased energy demand during differentiation [12,32,40–42]. Inhibition of mitochondrial dynamics by PI3K, JNK, and AMPK inhibitors (Fig. 6) further extends previous knowledge of their impact on the NGF differentiating activity. NGF signaling, known to control the expression of autophagy and fission–fusion proteins (Drp1, Opa1 and Mfn2) [7,12], also regulates mitochondrial integrity (Bcl-xL), stress responses (DJ-1 and SOD1), components of the mitophagy pathway (Parkin) and the dual role of Omi-HtrA2 in controlling both mitochondrial quality and caspase activation (Fig. 7). This is in agreement with the transcriptional control of these genes: SOD1, Parkin, HtrA2, DJ-1 and Ambra-1 [12] have binding sites for transcription factors, such as CREB, AP-1(FOS/JUN), NF-kB, that are induced by NGF [34,50–52], thereby improving current understanding of mechanisms underlying NGF-induced differentiation [3,24,32,53]. And, there is now an integral understanding, supported by a mathematical model (Fig. 5) that should enhance predictability and testability, and work in combination with our previous model of ROS management [54].

Another remarkable finding of this study is that NGF-mediated differentiation occurs with substantial metabolic remodeling, which affects energy transduction, anabolic processes, and components of the redox balance. Specifically, the NGF-mediated boost in all TCA cycle intermediates suggests and confirms our hypothesis that all mitochondrial and metabolic changes are needed to supply a higher amount of metabolic energy (ATP) for both morphological remodeling and for the novel neuronal functions. This new evidence also confirms our previous findings of an apparent energetic paradox, i.e. increased mitochondrial respiration with decreased ATP levels [12]. The human brain is about 2% of the total body weight, but accounts for 20% of total oxygen consumption, thus implying a 10-fold more intensive basal oxidative metabolism, 2/3 of which is pertinent to neurotransmission and synaptic functions. This concept has been confirmed in several models of brain development, both *in vivo* and *in vitro* [1,25,26,55], but we here show

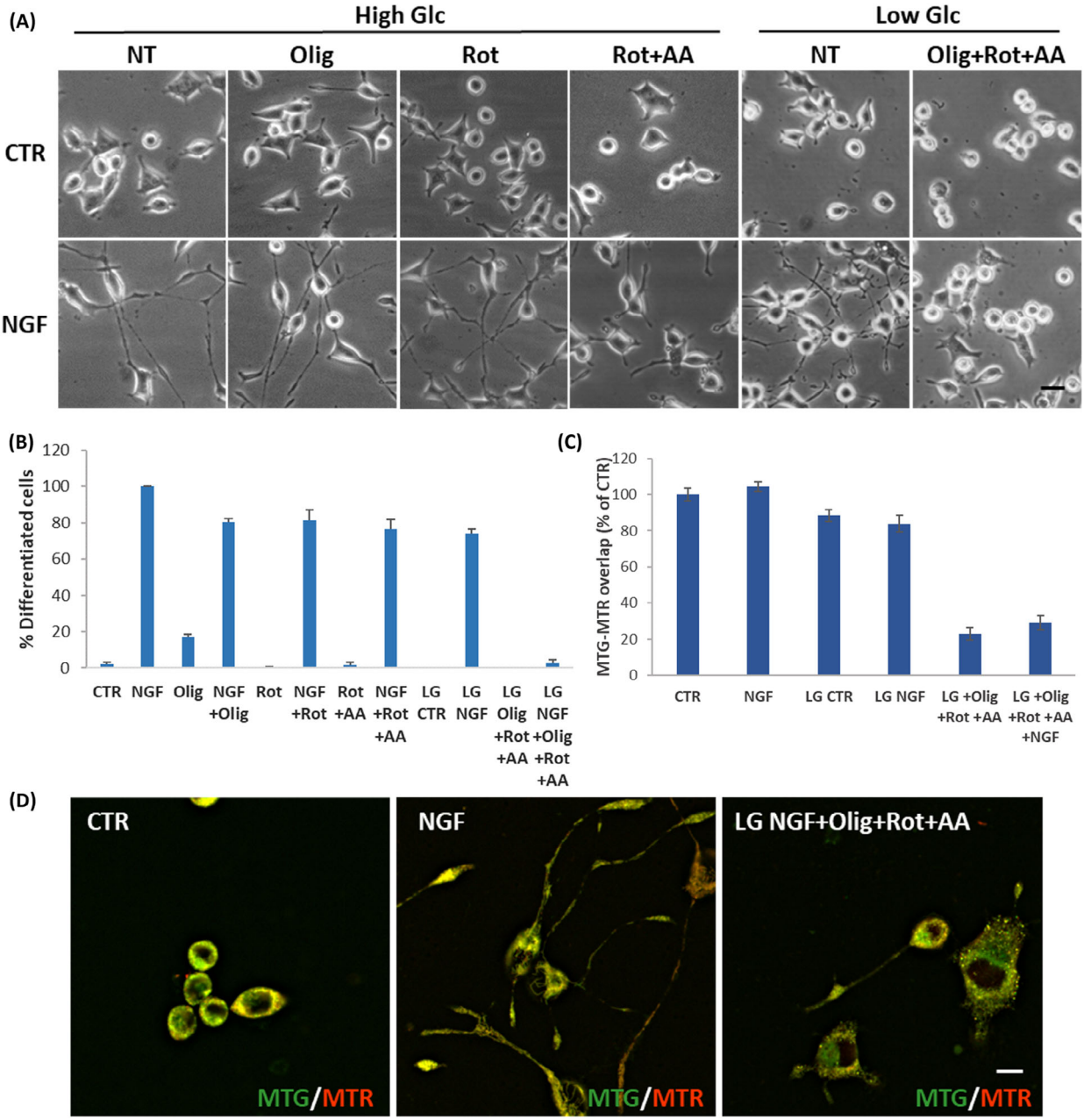

Fig. 9. Effect of low glucose (LG) and/or respiratory chain inhibitors on NGF differentiation and mitochondrial potential. (A, B) Representative images (A) and quantitation (B) of PC12 cells differentiation after NGF (10 ng·mL^{-1}) for 24 h and effect of low glucose (LG, 5 mM instead of 25 mM) and/or electron transport chain (ETC) inhibitors (Olig 1 μM, Rot 50 nM and AA 0.5 μM). Scale bar: 25 μm. Data are the mean ± SEM of three separate experiments, each performed in duplicate. (C) Quantitation of mitochondrial potential (MTR/MTG overlap) in PC12 treated with NGF for 24 h in normal medium (25 mM glucose) or LG (5 mM) and/or ETC inhibitors. Data, expressed as a percent of CTR ± SEM, are the mean of two experiments with duplicate samples. (D) Representative images of MTR/MTG-stained PC12 cells (merge images) exposed to NGF for 24 h and effect of LG plus the mixture of ETC. $N = 4$ for each treatment. Scale bar: 10 μm. AA, antimycin A; LG, low glucose; MTG, MitoTracker Green; MTR, MitoTracker Red CMXRos; NGF, nerve growth factor; Olig, oligomycin; Rot, rotenone.

that this glycolysis to respiration metabolic rewiring is induced by NGF, and thereby directly linked to the activity of one of the many neurotrophic factors controlling neuronal fate and development [33].

Nonetheless, the glycolysis to oxidative phosphorylation shift occurs with little changes in terms of glycolytic capacity, so cells maintain a certain degree of flexibility, at least during the first 24 h, before the full

post-mitotic state is established. In fact, cells are still able to have some differentiation also in low glucose medium, although to a smaller extent, perhaps thanks to the preferential use of the TCA cycle route. The use of TCA cycle and oxidative phosphorylation is functional to both obtaining more ATP from one single glucose molecule, and at the same time, conveying part of the glucose to the pentose phosphate pathway, which supports nucleotides and NADPH production, both important for anabolic processes.

While anabolic processes are sustained by using building blocks derived from the 1C metabolism [56], NADPH is also relevant for the reduction of oxidized GSSG to reduced GSH and for maintenance of redox homeostasis at increased ROS levels. This is a relevant aspect in neuronal physiology and brain homeostasis as the brain is a low-turnover tissue. The prevalently oxidative metabolism raises the chances to generate or overproduce ROS, whose accumulation would be deleterious for cells (neurons) that must persist for the entire lifetime of the organism. This problem may be controlled thanks to the highly efficient ROS scavenger systems, in particular GSH. Altogether, our findings show for the first time that the ability of NGF to induce a neuronal phenotype and to sustain its viability throughout the lifetime of the individual, may well be based on the ability of NGF to activate signaling pathways that coordinate and integrate all the processes that are required for differentiation, function, and maintenance. Enhanced mitochondrial cycling is one of these processes.

These findings may also have medical implications: Age-dependent reduction of NGF levels/signaling and of autophagy is inversely correlated to an increased risk of neurodegeneration, thus supporting the therapeutic potential of NGF [57]. Based on evidence that NGF-mediated neuroprotection also involves its antigliosis activity [58–60], it would be interesting to examine the connection between NGF-mediated regulation of metabolism in astrocytes, and neuronal susceptibility to neurodegeneration.

In conclusion, the experimental data in the present and the previous report [12] integrated through a new mathematical model of mitochondrial fusion–fission–mitophagy, provide a comprehensive paradigm in which mitochondrial fusion–fission–mitophagy cycling may help mitochondrial quality and the metabolic changes necessary for neuronal differentiation.

Materials and methods

Drugs and reagents

All cell culture reagents [Dulbecco's Modified Eagle's Medium (DMEM), Fetal Bovine Serum (FBS), Donor Horse Serum (HS), L-glutamine, Penicillin and Streptomycin] were purchased from Euroclone SpA (Milano, Italy). Poly-L-lysine was from SERVA Electrophoresis GmbH (Heidelberg, Germany). Murine 2.5S NGF (mNGF) was purchased from Promega Inc. (Madison, WI, USA). Nicotinamide adenine dinucleotide (NAD) was from Roche-Italia. Wortmannin (WT), Rapamycin (Rap), Bafilomycin A1 (Baf), Oligomycin A (Olig), Rotenone (Rot), Antimycin A (AA), and Hoechst 33342 were purchased from Sigma Aldrich/Merck (Burlington, MA, USA). JNK inhibitor II (SP600125) and Compound C (CC) were from Calbiochem (La Jolla, CA, USA). Dihydro-dichlorofluorescein diacetate (H_2DCF-DA), MitoTracker Red CMXRos (MTR), MitoTracker Green^{FM} (MTG) and LysoTrackerTM Red (LTR) were from ThermoFisher Scientific Life Technologies (Waltham, MA, USA).

Cell culture and treatments

PC12 cells (clone 615) (RRID:CVCL_C130) [61] (kindly provided by MV Chao, Skirball Institute, New York University School of Medicine, NY) were maintained in DMEM supplemented with 10% FBS, 5% heat-inactivated HS, 2 mM L-glutamine, 100 $\mu g \cdot mL^{-1}$ streptomycin, 100 $U \cdot mL^{-1}$ penicillin, in a humidified atmosphere of 95% air 5% CO_2 at 37 °C, as previously described [62–64]. Cells were routinely authenticated by immunoblot of the Tyrosine kinase receptor TrkA, as described [64]. All experiments were performed with mycoplasma-free cells (Mycoplasma qPCR Detection Kit; Sigma Aldrich/Merck). Medium was changed every other day and immediately before treatments. Drugs treatments: 2.5S mNGF (10 $ng \cdot mL^{-1}$), NAD^+ (100 μM), wortmannin (WT, 200 nM), compound C (CC, 10 μM), Rapamycin (Rap, 200 nM), Bafilomycin A1 (Baf, 100 nM), JNK inhibitor II (SP600125) (1 μM), Oligomycin A (Olig, 1 μM), complex I inhibitor rotenone (Rot, 50 nM) and complex III inhibitor Antimycin A (AA, 0.5 μM).

Mitochondrial function, morphology and mitophagy

Mitochondrial morphology (fragmented vs networked) and mitophagy were assessed by using MTG and LTR staining (Invitrogen). Briefly, cells (9×10^3/well) were plated in 96-multiwell plates (Perkin-Elmer, Waltham, MA, USA), previously coated with poly-L-lysine (10 $\mu g \cdot mL^{-1}$). For time-lapse imaging, cells were loaded with MTG (200 nM) and LTR (100 nM) for 15 min, and counterstained with Hoechst (1 $\mu g \cdot mL^{-1}$) [35]. Then, cells were rinsed twice with PBS, placed in DMEM without phenol red and exposed to NGF or NAD^+. Time-lapse imaging was performed during the 2–6 and 20–26 h timeframes of treatments. During the interval between the two time-lapse imaging sequences, plates were placed in the CO_2 incubator.

Images were acquired using Operetta® CLS (Perkin-Elmer Inc.), a high-content analysis system, with a 63×

water immersion objective. Images were analyzed using the HARMONY® software (Perkin-Elmer Inc.) to obtain quantitation of mitochondrial parameters. The following segmentation protocol was used: The software was instructed to recognize different classes of mitochondria (*i.e.* dispersed vs networked) based on specific morphology parameters (size, sphericity, length, volume) and SER texture (using the Line bright filter). Measured parameters include number of mitochondria, mean mitochondrial length (μm), total mitochondrial volume (μm^3), location in the cell (perinuclear vs neurite region, based on distance from nuclei). For mitophagy, the overlapping MTG-LTR spots were taken. All values were normalized by the total number of cells. Data are the mean of MTG spots/cell (for morphology), or overlapping MTG-LTR spots/cell (for mitophagy), on about 150 cells in 20 random imaged fields. Similar profiles were obtained in three independent experiments in duplicate.

To assess the mitochondrial potential, cells (1×10^4/well) were plated in glass bottom cell culture dishes (15 mm, NEST, Wuxi, China) previously coated with poly-L-lysine. Cells were loaded with MTR (50 nM) and MTG (200 nM) for 15 min, rinsed with PBS, placed in DMEM without phenol red and treated with NGF or NAD^+ for the indicated times (4–24–72 h). Live imaging was acquired using the Advanced Fluorescence THUNDER Imager Live Cell (LEICA Microsystem, Wetzlar, Germany) on about 100 cells for each condition in 10 random fields. Fluorescence intensity and the mitochondrial areas were quantified using IMAGEJ software (Bethesda, MD, USA).

ROS measurement

Cells (9×10^3/well) were plated in 96-multiwell plates (Euroclone) coated with poly-L-lysine and exposed to NGF ($10\ ng{\cdot}mL^{-1}$) or NAD^+ (100 μM) in DMEM w/o Phenol Red for 4–24–72 h. Cells were loaded with H_2DCFDA during the last 30 min, then detached, centrifuged at 600 *g*, resuspended in PBS and transferred into a black 96-multiwell plate (ThermoFisher Scientific Life Technologies). Fluorescence was measured using FLUOstar®Omega (BMG Labtech, Ortenberg, Germany) (excitation 485 nm, emission 520 nm). Values were normalized by MTT assay, as described in [63].

Cell morphology

To evaluate cell differentiation, PC12 cells (1×10^4/well) were plated in 24-multiwell plates (Euroclone), previously coated with poly-L-lysine, and treated with NGF ($10\ ng{\cdot}mL^{-1}$) or NAD^+ (100 μM) for the indicated times. Images were taken by using an Olympus CK40-SLP (Olympus, Tokyo, Japan) with a 20× objective. Differentiation was measured as percent of cells with neurite processes whose length is at least twice the diameter of the cell body. Number of differentiated cells and mean neurite length were measured on images using IMAGEJ software, as described [64].

For quantitative evaluation of morphology parameters, cells (9×10^3/well) were plated in 96-multiwell plates (Perkin-Elmer Inc.), previously coated with poly-L-lysine, and treated with NGF or NAD^+. Time-lapse imaging was performed during the 2–6 and 20–26 h timeframes of treatment. Images were acquired using Operetta® CLS (Perkin-Elmer Inc.) with a 63× water immersion objective in bright-field microscopy. Images of PC12 cells were analyzed using Harmony® software to obtain morphological parameters, such as surface area and sphericity of cells. Parallel cultures stained with Hoechst ($1\ \mu g{\cdot}mL^{-1}$) were used to measure nuclear morphology and apoptotic nuclei.

Immunocytochemistry

PC12 cells were grown onto 12 mm poly-L-lysine-coated coverslips (2×10^4 cells per well) and differentiated with NGF for 4 or 24 h [12]. Cells were then washed with PBS, fixed, permeabilized with 0.25% Triton X100 in PBS and incubated with the blocking solution (10% normal goat serum, Cell Signaling Technologies, Boston, MA, USA), followed by overnight incubation with the primary antibodies rabbit DJ-1 (D29E5) XP® (1 : 100, Cell Signaling Technologies), rabbit Omi-HtrA2 (1 : 100, Cell Signaling Technologies) and mouse TOMM20 (1 : 200, Abcam). After washing with PBS, coverslips were incubated for 2 h at room temperature with goat anti-rabbit Alexa 488™ and anti-mouse Alexa 546™ conjugated antibodies (1 : 500; ThermoFisher Scientific Life Technologies). Nuclei were counterstained with Hoechst 33342 ($1\ \mu g{\cdot}mL^{-1}$) for 15 min. After washes, coverslips were mounted with Dako Fluorescent Mounting Medium (Dako Agilent Technologies, Santa Clara, CA, USA) and visualized under the Advanced Fluorescence THUNDER Imager Live Cell (LEICA Microsystem). Images of about 100 cells were taken in ten random fields for each condition. Colocalization was determined by using the Pearson coefficient of correlation.

Western blot analysis

Total cell extracts and western blotting were performed as previously described [12]. Briefly, cells were washed in ice-cold PBS and scraped in lysis buffer (20 mM Tris pH 8.0; 137 mM NaCl; 1% Nonidet-P40; 10% glycerol; 1 mM DTT) containing proteases and phosphatases inhibitors (Cell Signaling Technologies). After 20 min incubation on ice, cellular debris were pelleted by centrifugation at 14 000 ***g*** for 10 min at 4 °C. Protein concentration was measured by using the Bradford assay (Sigma Aldrich/Merck).

Total proteins (25 μg) were dissolved in loading buffer (50 mM Tris pH 6.8; 2% SDS; 100 mM DTT, 10% glycerol, 0.1% bromophenol blue), separated on 10% SDS/PAGE gels and transferred to nitrocellulose Protran™ (Perkin-

Elmer Inc.). After blocking with 5% non-fat milk or BSA in TBST buffer (10 mM Tris pH 7.5; 150 mM NaCl; 0.2% Tween-20), blots were probed overnight at 4 °C with the primary antibody in TBST: mouse β3-Tubulin (1 : 1000; Cell Signaling Technologies), mouse GAP-43 (1 : 1000, Sigma Aldrich/Merck), rabbit Bcl-xL (1 : 1000; Cell Signaling Technologies), rabbit Omi-HtrA2 (1 : 500, Cell Signaling Technologies), mouse Parkin (1 : 100, Cell Signaling Technologies), mouse SOD1 (1 : 500, Millipore), rabbit TOMM20 (1 : 200, Immunological Sciences), rabbit Phospho(Thr183/Tyr185)-SAPK/JNK (1 : 1000, Cell Signaling Technologies), rabbit total JNK (1 : 1000, Cell Signaling Technologies), mouse β-actin (1 : 1000, Cell Signaling Technologies). For co-immunoprecipitation, total proteins (100 μg) were incubated with rabbit AMBRA1 (5 μL of 200 ng·μL^{-1}, Santa Cruz Biotechnology Inc., Dallas TX, USA) overnight at 4 °C. After separation with proteinA agarose for 2 h at 4 °C, and separation on 10% SDS/PAGE, membranes were probed with mouse Parkin (1 : 100, Invitrogen/Thermo Fisher Scientific Life Technologies). For detection, membranes were incubated for 1 h at RT with HRP-conjugated donkey anti-rabbit or anti-mouse IgGs (1 : 5000; Cell Signaling Technologies). Blots were probed for β-actin to normalize for protein content. Detection was carried out by chemiluminescence using SuperSignalTM West Pico PLUS Chemiluminescent Substrate (ThermoFisher Scientific Life Technologies). Quantification of bands was performed by densitometry using NIH-IMAGEJ software.

Metabolic profiling

PC12 cells (3×10^4/well) were plated in 6-well plates (Euroclone), previously coated with poly-L-lysine (10 μg·mL^{-1}) and treated with NGF (10 ng·mL^{-1}) for 4 or 24 h in complete growth medium (high glucose, 25 mM). At the end of treatments, metabolites extraction was performed as previously detailed in [65,66]. For metabolic profiling, samples were separated through an InfintyLab Poroshell 120 PFP column (2.1 × 100 mm, 2.7 μm) coupled to an Agilent 1290 Infinity UHPLC system (Agilent Technologies, Santa Clara, CA, USA) as described [65]. MS detection was performed using an Agilent 6550 iFunnel Q-TOF mass spectrometer with the Dual JetStream source operating in negative ionization mode (Agilent Technologies). Data analysis was performed with MassHunter ProFinder and MassHunter VistaFlux software (Agilent Technologies) as in [65,66].

Modeling

For computational modeling, the scheme in Fig. 5A was translated into mathematical equations (listed in the Table in the Appendix S1: Computational Modeling). The mathematical model was integrated in the Copasi software to run the simulations. The model instantiations used to run the simulations (Fig. 5) can be found in the Appendix S1 as Copasi files named 'Fig. 5.cps' (Appendix S1: Copasi models folder). The rate constants are found under Global Quantities in the model 'Fig. 5.cps'. To reproduce the simulations of Fig. 5, run the correspondent Copasi file contained in the folder 'fusion fission models', as detailed in the Instruction.

Statistical analysis

All data are presented as the mean ± SEM of three separate experiments with two independent samples ($N = 6$). Statistical analysis was performed by using GRAPHPAD PRISM 6.0 (GraphPad Software, La Jolla, CA, USA). All quantitative data were analyzed by one-way ANOVA and Dunnett's multiple comparisons test for multiple treatments (*$P \leq 0.05$, **$P \leq 0.01$, ***$P \leq 0.001$, ****$P \leq 0.0001$ *versus* the corresponding CTR). For the figures of ICC, individual images of CTR and treated cells were assembled and the same adjustments were made for brightness, contrast, and sharpness using ADOBE PHOTOSHOP (Adobe Systems, San Jose, CA, USA).

Acknowledgements

This work was supported by grants from the Italian Ministry of University and Research (MIUR) [PRIN2007 to AMC and MP; ISBE-SYSBIONET–Italian Roadmap of European Strategy Forum on Research Infrastructures (ESFRI) to LA (MP and AMC as Participants); SYSBIO-ISBE.ITALY; Italian Technological National Cluster Life-Science ALISEI–CTN01_00177_165430 IVASCOMAR to AMC; MUR-Competitive Grant for Excellent Department (2018–2022) to the Dept of Biotechnology and Biosciences, University Milano-Bicocca]; Netherlands Organization for Scientific Research (NWO) in the integrated program of WOTRO [W01.65.324.00/project 4] Science for Global Development to HVW; Synpol: EU-FP7 [KBBE.2012.3.4-02 #311815] to HVW; EU-CORBEL (Coordinated Research Infrastructures Building Enduring Life-science Services) [PID 2354] to HVW and AMC; EU-H2020 [NFRADEV-4-2014-2015#654248] to HVW; Epipredict: EU-H2020 MSCA-ITN-2014-ETN; Marie Skłodowska-Curie Innovative Training Networks (ITN-ETN) [#642691] to HVW; and BBSRC China [BB/J020060/1] to HVW. This work was also supported by Associazione Levi-Montalcini (fellowship to CG); Regione Lombardia "Innovazione, nuovi modelli Tecnologici e Reti per curare la SLA" (INTERSLA, ID 1157625) POR FESR 2014–2020 to NS and ELIXIR-IT through ELIXIRNextGenIT (Grant Code IR0000010) to MB. The research leading to these results has received funding from the European Union –

NextGenerationEU through the Italian Ministry of University and Research under PNRR – M4C2-I1.3 Project PE_00000019 "HEAL ITALIA" to AMC (BTBS-UNIMIB). The views and opinions expressed are those of the authors only and do not necessarily reflect those of the European Union or the European Commission. Neither the European Union nor the European Commission can be held responsible for them.

Conflict of interest

The authors declare no conflict of interest.

Author contributions

Conceptualization: AMC, LA, HVW; Methodology: AMC, HVW; Software: HVW, EW-T, CG, YL, IG, AV, DG and CD; Investigation: HVW, AMC, EW-T, YL, IG, CG, DG, MB, NS; Writing—Original Draft: AMC, HVW, MP; Writing—Review & Editing: AMC, HVW, LA, IG, CG, EW-T, MP, AV, CD, and DG; Funding Acquisition: AMC, LA, MP, HVW.

Computational modeling

Raw data, instructions, and recipes/Global quantities for the Copasi simulations (GitHub: https://github.com/HVWesterhoff/mitocycling/tree/main [reference number: github_westerhoff]), including: the computational modeling; a list and description of the equations used to model and quantify the concentrations of mitochondria, ROS, mitochondrial fractions, and cycling constants; the Copasi models in the 'fusion fission models' folder (the Copasi 'fusion fission model' and the Copasi 'fusion fission model_bis' for the simulations with distinct fission rate k).

Data availability statement

The data that support the findings of this study are openly available in GitHub: https://github.com/HVWesterhoff/mitocycling/tree/main [reference number: github_westerhoff].

References

1 Khacho M, Harris R & Slack RS (2019) Mitochondria as central regulators of neural stem cell fate and cognitive function. *Nat Rev Neurosci* **20**, 34–48.
2 Iwata R, Casimir P & Vanderhaeghen P (2020) Mitochondrial dynamics in postmitotic cells regulate neurogenesis. *Science* **369**, 858–862.
3 Li H, Chen Y, Jones AF, Sanger RH, Collis LP, Flannery R, McNay EC, Yu T, Schwarzenbacher R, Bossy B *et al.* (2008) Bcl-xL induces Drp1-dependent synapse formation in cultured hippocampal neurons. *Proc Natl Acad Sci USA* **105**, 2169–2174.
4 Ishihara N, Nomura M, Jofuku A, Kato H, Suzuki SO, Masuda K, Otera H, Nakanishi Y, Nonaka I, Goto YI *et al.* (2009) Mitochondrial fission factor Drp1 is essential for embryonic development and synapse formation in mice. *Nat Cell Biol* **11**, 958–966.
5 Wakabayashi J, Zhang Z, Wakabayashi N, Tamura Y, Fukaya M, Kensler TW, Iijima M & Sesaki H (2009) The dynamin-related GTPase Drp1 is required for embryonic and brain development in mice. *J Cell Biol* **186**, 805–816.
6 Rabinowitz JD & White E (2010) Autophagy and metabolism. *Science* **330**, 1344–1348.
7 Armijo-Weingart L, Ketschek A, Sainath R, Pacheco A, Smith GM & Gallo G (2019) Neurotrophins induce fission of mitochondria along embryonic sensory axons. *elife* **8**, 1–29.
8 Lou G, Palikaras K, Lautrup S, Scheibye-Knudsen M, Tavernarakis N & Fang EF (2020) Mitophagy and neuroprotection. *Trends Mol Med* **26**, 8–20.
9 Palikaras K & Tavernarakis N (2020) Regulation and roles of mitophagy at synapses. *Mech Ageing Dev* **187**, 111216.
10 Westermann B (2010) Mitochondrial fusion and fission in cell life and death. *Nat Rev Mol Cell Biol* **11**, 872–884.
11 Youle RJ & Van Der Bliek AM (2012) Mitochondrial fission, fusion, and stress. *Science* **337**, 1062–1065.
12 Martorana F, Gaglio D, Bianco MR, Aprea F, Virtuoso A, Bonanomi M, Alberghina L, Papa M & Colangelo AM (2018) Differentiation by nerve growth factor (NGF) involves mechanisms of crosstalk between energy homeostasis and mitochondrial remodeling. *Cell Death Dis* **9**, 1–16.
13 Lemasters JJ (2005) Selective mitochondrial autophagy, or mitophagy, as a targeted defense against oxidative stress, mitochondrial dysfunction, and aging. *Rejuvenation Res* **8**, 3–5.
14 Kim I, Rodriguez-Enriquez S & Lemasters JJ (2007) Selective degradation of mitochondria by mitophagy. *Arch Biochem Biophys* **462**, 245–253.
15 Scherz-Shouval R & Elazar Z (2007) ROS, mitochondria and the regulation of autophagy. *Trends Cell Biol* **17**, 422–427.
16 Ashrafi G & Schwarz TL (2013) The pathways of mitophagy for quality control and clearance of mitochondria. *Cell Death Differ* **20**, 31–42.
17 Geisler S, Holmström KM, Skujat D, Fiesel FC, Rothfuss OC, Kahle PJ & Springer W (2010) PINK1/Parkin-mediated mitophagy is dependent on VDAC1 and p62/SQSTM1. *Nat Cell Biol* **12**, 119–131.

18 Van Humbeeck C, Cornelissen T & Vandenberghe W (2011) Ambra1: a Parkin-binding protein involved in mitophagy. *Autophagy* **7**, 1555–1556.
19 Eiyama A & Okamoto K (2015) PINK1/Parkin-mediated mitophagy in mammalian cells. *Curr Opin Cell Biol* **33**, 95–101.
20 Pickrell AM & Youle RJ (2015) The roles of PINK1, Parkin, and mitochondrial fidelity in parkinson's disease. *Neuron* **85**, 257–273.
21 Choi GE, Lee HJ, Chae CW, Cho JH, Jung YH, Kim JS, Kim SY, Lim JR & Han HJ (2021) BNIP3L/NIX-mediated mitophagy protects against glucocorticoid-induced synapse defects. *Nat Commun* **12**, 487.
22 Ng MYW, Wai T & Simonsen A (2021) Quality control of the mitochondrion. *Dev Cell* **56**, 881–905.
23 Rolland SG & Conradt B (2010) New role of the BCL2 family of proteins in the regulation of mitochondrial dynamics. *Curr Opin Cell Biol* **22**, 852–858.
24 Kieper N, Holmström KM, Ciceri D, Fiesel FC, Wolburg H, Ziviani E, Whitworth AJ, Martins LM, Kahle PJ & Krüger R (2010) Modulation of mitochondrial function and morphology by interaction of Omi/HtrA2 with the mitochondrial fusion factor OPA1. *Exp Cell Res* **316**, 1213–1224.
25 Agostini M, Romeo F, Inoue S, Niklison-Chirou MV, Elia AJ, Dinsdale D, Morone N, Knight RA, Mak TW & Melino G (2016) Metabolic reprogramming during neuronal differentiation. *Cell Death Differ* **23**, 1502–1514.
26 Zheng X, Boyer L, Jin M, Mertens J, Kim Y, Ma L, Ma L, Hamm M, Gage FH & Hunter T (2016) Metabolic reprogramming during neuronal differentiation from aerobic glycolysis to neuronal oxidative phosphorylation. *elife* **5**, 1–25.
27 Colangelo A, Cirillo G, Alberghina L, Papa M & Westerhoff H (2019) Neural plasticity and adult neurogenesis: the deep biology perspective. *Neural Regen Res* **14**, 201–205.
28 Held NM & Houtkooper RH (2015) Mitochondrial quality control pathways as determinants of metabolic health. *BioEssays* **37**, 867–876.
29 Levi-Montalcini R (1952) Effects of mouse tumor transplantation on the nervous system. *Ann N Y Acad Sci* **55**, 330–344.
30 Mobley WC, Rutkowski JL, Tennekoon GI, Gemski J, Buchanan K & Johnston MV (1986) Nerve growth factor increases choline acetyltransferase activity in developing basal forebrain neurons. *Mol Brain Res* **387**, 53–62.
31 Alberghina L & Colangelo AM (2006) The modular systems biology approach to investigate the control of apoptosis in Alzheimer's disease neurodegeneration. *BMC Neurosci* **7**, 1–26.
32 Bianco MR, Berbenni M, Amara F, Viggiani S, Fragni M, Galimberti V, Colombo D, Cirillo G, Papa M, Alberghina L *et al.* (2011) Cross-talk between cell cycle induction and mitochondrial dysfunction during oxidative stress and nerve growth factor withdrawal in differentiated PC12 cells. *J Neurosci Res* **89**, 1302–1315.
33 Scardigli R, Capelli P, Vignone D, Brandi R, Ceci M, La Regina F, Piras E, Cintoli S, Berardi N, Capsoni S *et al.* (2014) Neutralization of nerve growth factor impairs proliferation and differentiation of adult neural progenitors in the subventricular zone. *Stem Cells* **32**, 2516–2528.
34 Rojo AI, Salinas M, Martín D, Perona R & Cuadrado A (2004) Regulation of Cu/Zn-superoxide dismutase expression via the phosphatidylinositol 3 kinase/Akt pathway and nuclear factor-κB. *J Neurosci* **24**, 7324–7334.
35 Klionsky DJ, Abdel-Aziz AK, Abdelfatah S, Abdellatif M, Abdoli A, Abel S, Abeliovich H, Abildgaard MH, Abudu YP, Acevedo-Arozena A *et al.* (2021) Guidelines for the use and interpretation of assays for monitoring autophagy (4th edition)[1]. *Autophagy* **17**, 1–382.
36 Mauro-Lizcano M, Esteban-Martínez L, Seco E, Serrano-Puebla A, Garcia-Ledo L, Figueiredo-Pereira C, Vieira HLA & Boya P (2015) New method to assess mitophagy flux by flow cytometry. *Autophagy* **11**, 833–843.
37 Mito T, Vincent AE, Faitg J, Taylor RW, Khan NA, McWilliams TG & Suomalainen A (2022) Mosaic dysfunction of mitophagy in mitochondrial muscle disease. *Cell Metab* **34**, 197–208.e5.
38 Huang X, Guo H, Cheng X, Zhang J, Qu W, Ding Q, Sun Q, Shu Q & Li X (2022) NAD + modulates the proliferation and differentiation of adult neural stem/progenitor cells via Akt signaling pathway. *Cell* **11**, 1283.
39 Hoops S, Sahle S, Gauges R, Lee C, Pahle J, Simus N, Singhal M, Xu L, Mendes P & Kummer U (2006) COPASI–a COmplex PAthway SImulator. *Bioinformatics* **22**, 3067–3074.
40 Posern G, Saffrich R, Ansorge W & Feller SM (2000) Rapid lamellipodia formation in nerve growth factor-stimulated PC12 cells is dependent on Rac and PI3K activity. *J Cell Physiol* **183**, 416–424.
41 Minden A, Lin A, McMahon M, Lange-Carter C, Dérijard B, Davis RJ, Johnson GL & Karin M (1994) Differential activation of ERK and JNK mitogen-activated protein kinases by Raf-1 and MEKK. *Science* **266**, 1719–1723.
42 Waetzig V & Herdegen T (2003) A single c-Jun N-terminal kinase isoform (JNK3-p54) is an effector in both neuronal differentiation and cell death. *J Biol Chem* **278**, 567–572.
43 Guo B, Liang Q, Li L, Hu Z, Wu F, Zhang P, Ma Y, Zhao B, Kovács AL, Zhang Z *et al.* (2014) O-GlcNAc-modification of SNAP-29 regulates autophagosome maturation. *Nat Cell Biol* **16**, 1215–1226.

44 Lee BE, Kim HY, Kim HJ, Jeong H, Kim BG, Lee HE, Lee J, Kim HB, Lee SE, Yang YR *et al.* (2020) O-GlcNAcylation regulates dopamine neuron function, survival and degeneration in Parkinson disease. *Brain* **143**, 3699–3716.
45 Lee BE, Suh PG & Kim JI (2021) O-GlcNAcylation in health and neurodegenerative diseases. *Exp Mol Med* **53**, 1674–1682.
46 Calissano P, Volontè C, Biocca S & Cattaneo A (1985) Synthesis and content of a DNA-binding protein with lactic dehydrogenase activity are reduced by nerve growth factor in the neoplastic cell line PC12. *Exp Cell Res* **161**, 117–129.
47 Bonnefont J & Vanderhaeghen P (2021) Neuronal fate acquisition and specification: time for a change. *Curr Opin Neurobiol* **66**, 195–204.
48 Brady NR, Elmore SP, Van Beek JJHGM, Krab K, Courtoy PJ, Hue L & Westerhoff HV (2004) Coordinated behavior of mitochondria in both space and time: a reactive oxygen species-activated wave of mitochondrial depolarization. *Biophys J* **87**, 2022–2034.
49 Brady NR, Hamacher-Brady A, Westerhoff HV & Gottlieb RA (2006) A wave of reactive oxygen species (ROS)-induced ROS release in a sea of excitable mitochondria. *Antioxid Redox Signal* **8**, 1651–1665.
50 Riccio A, Ahn S, Davenport CM, Blendy JA & Ginty DD (1999) Mediation by a CREB family transcription factor of NGF-dependent survival of sympathetic neurons. *Science* **286**, 2358–2361.
51 Boss V, Roback JD, Young AN, Roback LJ, Vogt Weisenhorn DM, Medina-Flores R & Wainer BH (2001) Nerve growth factor, but not epidermal growth factor, increases Fra-2 expression and alters Fra-2/JunD binding to AP-1 and CREB binding elements in pheochromocytoma (PC12) cells. *J Neurosci* **21**, 18–26.
52 Mullenbrock S, Shah J & Cooper GM (2011) Global expression analysis identified a preferentially nerve growth factor-induced transcriptional program regulated by sustained mitogen-activated protein kinase/extracellular signal-regulated kinase (ERK) and AP-1 protein activation during PC12 cell dif. *J Biol Chem* **286**, 45131–45145.
53 Vyas S, Juin P, Hancock D, Suzuki Y, Takahashi R, Triller A & Evan G (2004) Differentiation-dependent sensitivity to apoptogenic factors in PC12 cells. *J Biol Chem* **279**, 30983–30993.
54 N Kolodkin A, Sharma RP, Colangelo AM, Ignatenko A, Martorana F, Jennen D, Briedé JJ, Brady N, Barberis M, Mondeel TDGA *et al.* (2020) ROS networks: designs, aging, Parkinson's disease and precision therapies. *NPJ Syst Biol Appl* **6**, 34.
55 Herrero-Mendez A, Almeida A, Fernández E, Maestre C, Moncada S & Bolaños JP (2009) The bioenergetic and antioxidant status of neurons is controlled by continuous degradation of a key glycolytic enzyme by APC/C-Cdh1. *Nat Cell Biol* **11**, 747–752. doi: 10.1038/ncb1881
56 Ducker GS & Rabinowitz JD (2017) One-carbon metabolism in health and disease. *Cell Metab* **25**, 27–42.
57 Tuszynski MH, Thal L, Pay M, Salmon DP, Sang UH, Bakay R, Patel P, Blesch A, Vahlsing HL, Ho G *et al.* (2005) A phase 1 clinical trial of nerve growth factor gene therapy for Alzheimer disease. *Nat Med* **11**, 551–555.
58 Colangelo AM, Cirillo G, Lavitrano ML, Alberghina L & Papa M (2012) Targeting reactive astrogliosis by novel biotechnological strategies. *Biotechnol Adv* **30**, 261–271. doi: 10.1016/j.biotechadv.2011.06.016
59 Cirillo G, Colangelo AM, De Luca C, Savarese L, Barillari MR, Alberghina L & Papa M (2016) Modulation of matrix metalloproteinases activity in the ventral horn of the spinal cord re-stores neuroglial synaptic homeostasis and neurotrophic support following peripheral nerve injury. *PLoS One* **11**, 1–12.
60 Virtuoso A, Colangelo AM, Korai SA, Izzo S, Todisco A, Giovannoni R, Lavitrano M, Papa M & Cirillo G (2021) Inhibition of plasminogen/plasmin system retrieves endogenous nerve growth factor and adaptive spinal synaptic plasticity following peripheral nerve injury. *Neurochem Int* **148**, 105113.
61 Hempstead BL, Rabin SJ, Kaplan L, Reid S, Parada LF & Kaplant DR (1992) Overexpression of the trk tyrosine kinase rapidly accelerates nerve growth factor-induced differentiation. *Neuron* **9**, 883–896.
62 Amara F, Berbenni M, Fragni M, Leoni G, Viggiani S, Ippolito VM, Larocca M, Rossano R, Alberghina L, Riccio P *et al.* (2015) Neuroprotection by cocktails of dietary antioxidants under conditions of nerve growth factor deprivation. *Oxidative Med Cell Longev* **2015**, 1–15.
63 Martorana F, Foti M, Virtuoso A, Gaglio D, Aprea F, Latronico T, Rossano R, Riccio P, Papa M, Alberghina L *et al.* (2019) Differential modulation of NF-κ B in neurons and astrocytes underlies neuroprotection and Antigliosis activity of natural antioxidant molecules. *Oxidative Med Cell Longev* **2019**, 1–16.
64 Colangelo AM, Finotti N, Ceriani M, Alberghina L, Martegani E, Aloe L, Lenzi L & Levi-Montalcini R (2005) Recombinant human nerve growth factor with a marked activity in vitro and in vivo. *Proc Natl Acad Sci USA* **102**, 18658–18663.
65 Bonanomi M, Salmistraro N, Fiscon G, Conte F, Paci P, Bravatà V, Forte GI, Volpari T, Scorza M, Mastroianni F *et al.* (2021) Transcriptomics and metabolomics integration reveals redox-dependent metabolic rewiring in breast cancer cells. *Cancers (Basel)* **13**, 1–22.
66 Bonanomi M, Salmistraro N, Porro D, Pinsino A, Colangelo AM & Gaglio D (2022) Polystyrene micro and nano-particles induce metabolic rewiring in normal human colon cells: a risk factor for human health. *Chemosphere* **303**, 134947.

Supporting information

Additional supporting information may be found online in the Supporting Information section at the end of the article.

Video S1. Live imaging of PC12 differentiated with NGF for 24 h (1-NGF_24h).

Video S2. Live imaging of PC12 exposed to NGF for 24 h (NGF_24h_detail).

Video S3. Live imaging of PC12 without treatment (CTR).

Appendix S1. Computational Modeling: Raw data, instructions and recipes/Global quantities for the Copasi simulations.